Understanding the Regeneration Stage Undergone by Surface Cyclones Crossing a Midlatitude Jet in a Two-Layer Model

GWENDAL RIVIÈRE

CNRM/GAME, Météo-France/CNRS, Toulouse, France

JEAN-BAPTISTE GILET

Woods Hole Oceanographic Institution, Woods Hole, Massachusetts

LUDIVINE ORUBA

Laboratoire de Météorologie Dynamique/IPSL, ENS/CNRS/UPMC, Paris, France

(Manuscript received 14 December 2012, in final form 16 February 2013)

ABSTRACT

The present paper provides a rationale for the regeneration stage undergone by surface cyclones when they cross a baroclinic jet from its anticyclonic-shear (warm) side to its cyclonic-shear (cold) side in a two-layer quasigeostrophic model. To do so, the evolution of finite-amplitude synoptic cyclones in various baroclinic zonal flows is analyzed.

Baroclinic zonal flows with uniform horizontal shears are first considered. While the anticyclonic shear allows a much more efficient and sustainable extraction of potential energy than the cyclonic shear, the growth of the lower-layer eddy kinetic energy (EKE) is shown to be highly dependent on the choice of the parameter values. An increased vertical shear leads to a more rapid EKE increase in the anticyclonic shear than in the cyclonic shear whereas increasing the vertically averaged potential vorticity gradient or the barotropic shear stabilizes the EKE more in the former shear than in the latter. Finally, vertical velocities arising from the nonlinear interaction between synoptic cyclones are shown to favor EKE growth in the cyclonic shear rather than in the anticyclonic one.

The evolution of cyclones initialized on the warm side of a meridionally confined baroclinic jet is then investigated. The lower-layer cyclone crosses the jet axis and undergoes two distinct growth stages. The first growth stage results from the classical baroclinic interaction and is mainly driven by linear interaction between the cyclones and the jet. The second growth stage is mainly a nonlinear process. It is triggered by the vertical velocities created by the three-dimensional structure of the cyclonic disturbances when they reach the cyclonic side of the jet.

1. Introduction

It is well known that extratropical cyclones develop by extracting energy from the available background potential energy through baroclinic interaction. The baroclinicity is the key parameter governing this interaction and is usually quantified by the Eady growth rate, which depends on the vertical shear of the background flow (Hoskins and Valdes 1990). However, numerous numerical studies have shown that the behavior of extratropical cyclones is modulated by the horizontal shears of the large-scale background flow (James 1987; Davies et al. 1991; Thorncroft et al. 1993; Wernli et al. 1998) as well as by its confluent and diffluent components (Cai and Mak 1990; Whitaker and Barcilon 1992; Schultz et al. 1998). Davies et al. (1991) and Thorncroft et al. (1993) investigated the nonlinear evolution of unstable normal modes in unsheared, cyclonically sheared, and anticyclonically sheared baroclinic zonal flows. Both the synoptic-scale structure of the disturbances and the fronts were shown to largely differ among the three cases. For instance, the cyclonic (anticyclonic) shear favors the formation of the warm (cold) front and the

Corresponding author address: Gwendal Rivière, Météo-France, CNRM/GMAP/RECYF, 42 av. G. Coriolis, 31057 Toulouse CEDEX 1, France.
E-mail: gwendal.riviere@meteo.fr

DOI: 10.1175/JAS-D-12-0345.1

intensification of low (high) pressure systems. Wernli et al. (1998) found similar results by initializing the models with localized finite-amplitude anomalies. Furthermore, the Norwegian cyclone model (Bjerknes and Solberg 1922) is found to appear in the cyclonic-shear case while the model of Shapiro and Keyser (1990) with a T-bone frontal structure dominates in unsheared cases. Despite all this information, it is still unclear which side of a baroclinic zonal jet is the more cyclogenetic. Indeed, even though the cyclonic side favors low pressure systems as previously recalled, this side is biased by the low pressure of the background environment and it is not clear if the perturbation low is deeper on the cyclonic side than on the anticyclonic side. The purpose of the present study is to numerically investigate this aspect within a quasigeostrophic framework by modifying the vertical and horizontal shears of the background flow as well as the scale and intensity of the synoptic disturbances in the initial conditions of the model.

Another motivation of the present study relies on the observations that most Atlantic storms that hit Europe undergo a rapid intensification stage during the crossing of the large-scale jet stream from its warm-air to its cold-air side—that is, from its anticyclonic to its cyclonic side (Baehr et al. 1999; Wernli et al. 2002; Rivière and Joly 2006; Pinto et al. 2009). Gilet et al. (2009) have recently shown that such a regeneration of a surface cyclone during the jet-crossing phase can be easily reproduced by performing idealized numerical experiments of a two-layer quasigeostrophic model on an f plane or a β plane. The simplest numerical configuration consists in initializing the model with localized finite-amplitude synoptic-scale cyclones on the anticyclonic side of a baroclinic zonal westerly jet. The key ingredient that allows a surface cyclone to move across the upper-level jet axis is the vertically averaged horizontal potential vorticity (PV) gradient (hereafter called the barotropic PV gradient). If the simulation is performed on an f plane with a pure baroclinic westerly jet without any barotropic component, the barotropic PV gradient is zero and the surface cyclone is not able to cross the upper-level jet axis. On the contrary, if the simulation is done on a β plane and/or with a westerly jet having a nonzero barotropic component, the barotropic PV gradient is poleward oriented and the displacement across the jet axis may occur. The cross-jet speed increases with an intensified poleward-oriented barotropic PV gradient. These results were interpreted as a generalization of the so-called β-drift mechanism in a midlatitude atmospheric context. Initially developed from a theoretical perspective by Rossby (1948) and Adem (1956), the β drift has been extensively studied to explain the behavior of tropical cyclones (e.g., Holland 1984; Moustaoui et al. 2002) and oceanic vortices (e.g., Morel and McWilliams 1997) and appears now as a key factor to explain the motion of midlatitude synoptic eddies such as surface cyclones (Gilet et al. 2009; Oruba et al. 2012, 2013) and upper-tropospheric anomalies (Rivière 2008). Note finally that this mechanism was recently confirmed in a much more realistic context by performing numerical sensitivity experiments of the Météo-France global operational forecast model for the particular case of the winter storm Xynthia that occurred at the end of February 2010 (Rivière et al. 2012).

Although the mechanism responsible for the motion of a surface cyclone across the upper-level jet axis was identified in the idealized simulations of Gilet et al. (2009) and Oruba et al. (2013) as explained above, the reason for the regeneration stage during the jet-crossing phase was not deeply investigated. The purpose of the present study is to provide a rationale for this growth stage using the same two-layer quasigeostrophic model as in the latter studies and by making kinetic energy budgets. In section 2, the model and energy budgets are presented as well as a detailed decomposition of the omega equation into linear and nonlinear terms. Section 3 is dedicated to simulations where the background flow is composed of uniform horizontal and vertical shears. Sensitivity experiments over a wide range of parameters are made to precisely diagnose the factors favoring the growth rates in anticyclonically sheared and cyclonically sheared baroclinic zonal flows. In section 4, the background flow is composed of a meridionally confined zonal jet and a detailed energy budget is made to identify the mechanism responsible for the regeneration stage of the lower-layer cyclones when they cross the jet axis and reach its cyclonic side. Finally, section 5 summarizes the results and provides a discussion.

2. Methodology

a. Model

The model is the two-layer quasigeostrophic model initially developed by Phillips (1951). The two discrete layers are contained between two rigid horizontal plates. The model conserves the PV in the lower layer (denoted with subscript l) and upper layer (denoted with subscript u). The prognostic equations can be expressed as

$$\frac{\partial q_k}{\partial t} + \mathbf{u}_k \cdot \nabla q_k = 0, \quad k \in [u, l], \tag{1}$$

where q_k is the PV in the layer k. The PV has the following expression:

TABLE 1. Summary of the different parameter values.

α	Standard velocity shear	$2.4 \times 10^{-5}\,\mathrm{s}^{-1}$
f_0	Uniform Coriolis parameter	$10^{-4}\,\mathrm{s}^{-1}$
β_0	Reference for the y derivative of f	$1.6 \times 10^{-11}\,\mathrm{m}^{-1}\,\mathrm{s}^{-1}$
λ	Rossby radius of deformation	$4.5 \times 10^{5}\,\mathrm{m}$

$$q_u = f + \Delta\psi_u - \lambda^{-2}(\psi_u - \psi_l), \tag{2}$$

$$q_l = f + \Delta\psi_l + \lambda^{-2}(\psi_u - \psi_l), \tag{3}$$

where Δ denotes the Laplacian operator. The streamfunction and geostrophic wind in the layer k are respectively denoted as ψ_k and $\mathbf{u}_k = (u_k, v_k)$. Also, λ denotes the Rossby radius of deformation and $f = f_0 + \beta y$ is the Coriolis parameter. As in Gilet et al. (2009) and Oruba et al. (2013), the model is spectral, and the nonlinear terms are computed on a regular grid. A leapfrog temporal scheme is used and the domain is biperiodic. The spatial and temporal resolutions are equal to $\delta x = \delta y = 125\,\mathrm{km}$ and $\delta t = 225\,\mathrm{s}$ and no diffusion is included in the following numerical experiments. Values of f_0 and λ are $10^{-4}\,\mathrm{s}^{-1}$ and 450 km, respectively (see Table 1). Depending on the simulations, β can be equal to β_0, a typical midlatitude value of the y derivative of f (see Table 1), or to $3\beta_0$ to represent the increased PV gradient in presence of meridionally confined westerly jets.

b. Omega and relative vorticity equations

The omega equation in the two-layer model on a β plane that determines the vertical velocity as function of the geostrophic variables can be expressed as

$$(\Delta - 2\lambda^{-2})(\lambda^{-1}s\omega_{u-l}) = -2\frac{\lambda^{-1}}{s}\nabla\cdot\mathbf{Q} - \lambda^{-2}\beta(v_u - v_l) = F, \tag{4}$$

where

$$\mathbf{Q} = (Q_x, Q_y) = -\lambda^{-1}s\left[\frac{1}{2}\frac{\partial(\mathbf{u}_u + \mathbf{u}_l)}{\partial x}\cdot\nabla(\psi_u - \psi_l), \frac{1}{2}\frac{\partial(\mathbf{u}_u + \mathbf{u}_l)}{\partial y}\cdot\nabla(\psi_u - \psi_l)\right] \tag{5}$$

is the so-called **Q** vector (Hoskins et al. 1978) and ω_{u-l} denotes the vertical velocity in pressure coordinates at the interface between the two layers. The quantity $s^2 \equiv -h(d\theta_R/dp)$ is a stratification parameter with θ_R being the reference potential temperature and with $h \equiv (R/p)(p/p_s)^{R/C_p}$. Note that λ and s are linked by the following relation: $\lambda^{-1}s = f_0/\delta p$, where f_0 is the Coriolis parameter and δp the difference of pressure between the middle of the two layers (Holton 1992).[1] Note finally that the sign of F, that is the right-hand side term of Eq. (4), determines that of the vertical velocity because $F > 0$ ($F < 0$) leads to updraft (downdraft).

In what follows, the total flow is decomposed into a zonal basic state (denoted with an overbar) and a perturbation (denoted with primes). The zonal basic flow depends only on latitude [$\overline{\mathbf{u}}_u = \overline{u}_u(y)\mathbf{i}$ and $\overline{\mathbf{u}}_l = \overline{u}_l(y)\mathbf{i}$] and is solution of Eq. (1). Hereafter $\mathbf{Q}^{\mathrm{lin}}$ and $\mathbf{Q}^{\mathrm{nl}}$ denote the linear and nonlinear parts of the **Q** vector, respectively, which can be written as

$$\mathbf{Q}^{\mathrm{lin}} \equiv -\lambda^{-1}s\left[\frac{1}{2}(-\overline{u}_u + \overline{u}_l)\frac{\partial}{\partial x}(v'_u + v'_l), \frac{1}{2}(-\overline{u}_u + \overline{u}_l)\frac{\partial}{\partial y}(v'_u + v'_l) + \frac{1}{2}(v'_u - v'_l)\frac{\partial}{\partial y}(\overline{u}_u + \overline{u}_l)\right], \tag{6}$$

$$\mathbf{Q}^{\mathrm{nl}} \equiv -\lambda^{-1}s\left[\frac{1}{2}\frac{\partial(\mathbf{u}'_u + \mathbf{u}'_l)}{\partial x}\cdot\nabla(\psi'_u - \psi'_l), \frac{1}{2}\frac{\partial(\mathbf{u}'_u + \mathbf{u}'_l)}{\partial y}\cdot\nabla(\psi'_u - \psi'_l)\right]. \tag{7}$$

The quantity F is also decomposed into a linear and a nonlinear part such that $F = F^{\mathrm{lin}} + F^{\mathrm{nl}}$. According to Eq. (4), the linear part of F contains a part without β, [$F_0^{\mathrm{lin}} \equiv -2(\lambda^{-1}/s)\nabla\cdot\mathbf{Q}^{\mathrm{lin}}$]; and another with β [$F_\beta^{\mathrm{lin}} \equiv -\lambda^{-2}\beta(v'_u - v'_l)$] and can be expressed as

$$F^{\mathrm{lin}} \equiv F_0^{\mathrm{lin}} + F_\beta^{\mathrm{lin}}, = -\lambda^{-2}\left\{\begin{array}{l}(\overline{u}_u - \overline{u}_l)\Delta(v'_u + v'_l) + \\ [\beta - \partial_y^2(\overline{u}_u + \overline{u}_l)](v'_u - v'_l) \\ -2\partial_y\overline{u}_l\partial_y v'_u + 2\partial_y\overline{u}_u\partial_y v'_l\end{array}\right\}. \tag{8}$$

The first term of the right-hand side (rhs) of Eq. (8) corresponds to the classical baroclinic term that creates updraft (downdraft) to the east (west) of a cyclone embedded in a positive vertical shear ($\overline{u}_u - \overline{u}_l > 0$). The second term corresponds to the impact of an effective β on the vertical velocity because it involves the barotropic PV gradient [$\beta - \partial_y^2(\overline{u}_u + \overline{u}_l)$]. The last two terms of the rhs of Eq. (8) involving the horizontal shears and their impact on the vertical velocity will be discussed later. Finally, the nonlinear part of F can be simply expressed as

$$F^{\mathrm{nl}} = -2\frac{\lambda^{-1}}{s}\nabla\cdot\mathbf{Q}^{\mathrm{nl}}. \tag{9}$$

[1] Note that here, λ has the dimension of a distance and is the multiplicative inverse of Holton (1992)'s λ.

The linearity of the relation between F and ω_{u-l} [see Eq. (4)] allows one to consider separately the vertical velocity fields induced by the forcings F^{lin} and F^{nl}. They will be hereafter denoted as $\omega^{\mathrm{lin}}_{u-l}$ and $\omega^{\mathrm{nl}}_{u-l}$ respectively.

The relative vorticity evolution in each layer (ζ_k) can be written as (Holton 1992)

$$\frac{\partial \zeta'_u}{\partial t} + \mathbf{u}'_u \cdot \nabla \overline{\zeta}_u + \overline{\mathbf{u}}_u \cdot \nabla \zeta'_u + \mathbf{u}'_u \cdot \nabla \zeta'_u + \beta v'_u = \lambda^{-1} s \omega'_{u-l}, \tag{10}$$

$$\frac{\partial \zeta'_l}{\partial t} + \mathbf{u}'_l \cdot \nabla \overline{\zeta}_l + \overline{\mathbf{u}}_l \cdot \nabla \zeta'_l + \mathbf{u}'_l \cdot \nabla \zeta'_l + \beta v'_l = -\lambda^{-1} s \omega'_{u-l}, \tag{11}$$

where $\lambda^{-1} s \omega'_{u-l}$ and $-\lambda^{-1} s \omega'_{u-l}$ are the two stretching terms $f_0 \partial \omega'/\partial p$ appearing in the upper-layer and lower-layer equations of the two-layer quasigeostrophic model. They are proportional to the vertical velocity at the interface between the two layers because the lowermost and uppermost frontiers of the model are rigid (Holton 1992). Suppose that an upper and a lower disturbance are in quadrature phase with each other and that the upper disturbance is to the west of the lower one. Where the lower disturbance reaches its minimum pressure (or maximum vorticity), $v'_l = 0$ and v'_u reaches a positive maximum. In midlatitudes, since the basic-state vertical shear $\overline{u}_u - \overline{u}_l$ is positive as well as the barotropic PV gradient $\beta - \partial^2_y(\overline{u}_u + \overline{u}_l)$, the first two terms on the rhs of Eq. (8) have opposite signs in that region, with the first one $[-\lambda^{-2}(\overline{u}_u - \overline{u}_l)\Delta v'_u]$ being positive and the second one $\{-\lambda^{-2}[\beta - \partial^2_y(\overline{u}_u - \overline{u}_l)]v'_u\}$ being negative. The effective beta term tends to reduce the ascending motion above the maximum vorticity of the lower-layer disturbance. This reduction in the vertical velocity reduces the positive stretching term in the lower-layer relative vorticity equation [see Eq. (11)] and reduces the relative vorticity growth of the lower-layer disturbance. On the contrary, where the upper disturbance reaches its minimum pressure (or maximum vorticity), $v'_u = 0$ and the first two terms on the rhs of Eq. (8) have the same sign and are both negative. These two terms tend to intensify the relative vorticity growth of the upper disturbance through the stretching term [see rhs of Eq. (10)]. Therefore, the effective beta term tends to create an asymmetry between the two layers, which is described in the next subsection from an energetic point of view.

c. Energy budget

Following Cai and Mak (1990), the time evolution of the perturbation kinetic energy $[K' \equiv (1/2)\mathbf{u}'^2_g]$ and potential energy $[P' \equiv (f_0^2/2s^2)(\partial \psi'/\partial p)^2]$ in quasigeostrophic equations can be expressed as

$$\frac{D_g K'}{Dt} = \mathbf{E} \cdot \mathbf{D} - \nabla \cdot (\mathbf{u}'_g p'_a + f_0 \psi' \nabla \chi') - f_0 \frac{\partial}{\partial p}(\omega' \psi') + f_0 \omega' \frac{\partial \psi'}{\partial p}, \tag{12}$$

$$\frac{D_g P'}{Dt} = -\frac{f_0^2}{s^2}\left(v'_g \frac{\partial \psi'}{\partial p}\frac{\partial^2 \overline{\psi}}{\partial y \partial p} + u'_g \frac{\partial \psi'}{\partial p}\frac{\partial^2 \overline{\psi}}{\partial x \partial p}\right) - f_0 \omega' \frac{\partial \psi'}{\partial p}, \tag{13}$$

where $D_g/Dt = \partial/\partial t + (\overline{\mathbf{u}}_g + \mathbf{u}'_g) \cdot \nabla$ denotes the Lagrangian geostrophic derivative. The p'_a and χ' represent respectively the perturbation ageostrophic pressure and velocity potential. They are both involved in the expression of the perturbation ageostrophic horizontal velocity $\mathbf{u}'_a = -(1/f_0)\mathbf{k} \times \nabla p'_a + \nabla \chi'$, where $\mathbf{k}$ is the vertical unit vector. The scalar product $\mathbf{E} \cdot \mathbf{D}$ is the barotropic energy conversion rate from the basic flow to the perturbation with $\mathbf{E}$ and $\mathbf{D}$ being defined as follows:

$$\mathbf{E} \equiv \left[\frac{1}{2}(v'^2_g - u'^2_g),\ -u'_g v'_g\right], \tag{14}$$

$$\mathbf{D} \equiv \left(\frac{\partial \overline{u}_g}{\partial x} - \frac{\partial \overline{v}_g}{\partial y}, \frac{\partial \overline{v}_g}{\partial x} + \frac{\partial \overline{u}_g}{\partial y}\right). \tag{15}$$

In the two-layer model, the kinetic energy equation at the two layers can be written as

$$\frac{D_g K'_l}{Dt} = \mathbf{E}_l \cdot \mathbf{D}_l - \nabla \cdot (\mathbf{u}'_l p'_{\mathrm{al}} + f_0 \psi'_l \nabla \chi'_l) + \lambda^{-1} s \omega'_{u-l} \frac{\psi'_u + \psi'_l}{2} - \lambda^{-1} s \omega'_{u-l} \frac{\psi'_u - \psi'}{2}, \tag{16}$$

$$\frac{D_g K'_u}{Dt} = \mathbf{E}_u \cdot \mathbf{D}_u - \nabla \cdot (\mathbf{u}'_u p'_{\mathrm{au}} + f_0 \psi'_u \nabla \chi'_u) - \lambda^{-1} s \omega'_{u-l} \frac{\psi'_u + \psi'_l}{2} - \lambda^{-1} s \omega'_{u-l} \frac{\psi'_u - \psi'_l}{2}, \tag{17}$$

and the potential energy equation at the interface between the two layers is

$$\frac{D_g P'}{Dt} = \frac{\lambda^{-2}}{2}[(v'_u + v'_l)(\overline{u}_u - \overline{u}_l) - (u'_u + u'_l)(\overline{v}_u - \overline{v}_l)] \times (\psi'_u - \psi'_l) + \lambda^{-1} s \omega'_{u-1}(\psi'_u - \psi'_l). \tag{18}$$

By integrating each equation over the whole domain (operation denoted as $\langle \cdot \rangle$), the advection terms included in the Lagrangian geostrophic time derivatives of Eqs. (16)–(18) and the horizontal redistribution terms that

are the second terms of the rhs of the same equations disappear. Therefore, we obtain

$$\frac{d}{dt}\langle K_l' \rangle = \langle \mathbf{E}_l \cdot \mathbf{D}_l \rangle + \langle \mathrm{CV} \rangle + \frac{\langle \mathrm{CI} \rangle}{2}, \tag{19}$$

$$\frac{d}{dt}\langle K_u' \rangle = \langle \mathbf{E}_u \cdot \mathbf{D}_u \rangle - \langle \mathrm{CV} \rangle + \frac{\langle \mathrm{CI} \rangle}{2}, \quad \text{and} \tag{20}$$

$$\frac{d}{dt}\langle P' \rangle = \langle \mathrm{CB} \rangle - \langle \mathrm{CI} \rangle, \tag{21}$$

where d/dt denotes the time derivative. In addition,

$$\mathrm{CI} = -\lambda^{-1} s \omega_{u-l}' (\psi_u' - \psi_l'), \tag{22}$$

$$\mathrm{CV} = \lambda^{-1} s \omega_{u-l}' \frac{(\psi_u' - \psi_l')}{2}, \tag{23}$$

$$\mathrm{CB} = \frac{\lambda^{-2}}{2}[(v_u' + v_l')(\overline{u}_u - \overline{u}_l) - (u_u' + u_l')(\overline{v}_u - \overline{v}_l)](\psi_u' - \psi_l'). \tag{24}$$

The quantity CI represents the internal conversion term [i.e., the energy transfer from eddy potential energy to eddy kinetic energy (EKE)]. Note that CI/2 appears on the rhs of the kinetic energy equation of each layer [Eqs. (19) and (20)] and is equivalent to the fourth term of the rhs of Eq. (12) within the two-layer framework. Note that −CI logically appears on the rhs of the potential energy equation at the interface [Eq. (21)]. The quantity CB is the baroclinic conversion term (i.e., the baroclinic energy transfer from the basic-state potential energy to eddy potential energy) and is the two-layer formulation of the first term of the rhs of Eq. (13). It is only involved in the potential energy equation at the interface [Eq. (21)]. The quantity CV is the two-layer formulation of the convergence of the vertical ageostrophic fluxes [third term on the rhs of Eq. (12)]. It corresponds to the exchanges of kinetic energy between the two layers since CV and −CV appear respectively in Eqs. (19) and (20). Note finally that the sum of CV and CI/2 is simply the product of the stretching term by the perturbation streamfunction $-f_0(\partial\omega'/\partial p)\psi'$ and has the following expression at the lower layer:

$$\mathrm{CV} + \frac{\mathrm{CI}}{2} = \lambda^{-1} s \omega_{u-l}' \psi_l'. \tag{25}$$

When the two fields are anticorrelated (strong ascending motions above the lower-layer cyclone), CV + CI/2 reaches large positive values. Our study is hereafter focused on the lower-layer kinetic energy (EKE) evolution as diagnosed from Eq. (19).

d. Disturbances

The perturbation streamfunction ψ_k' in each layer k has a Gaussian elliptic shape and is defined as

$$\psi_k' = A' \exp\left\{ \begin{array}{l} -\dfrac{[(x - x_{0k})\cos\phi' + (y - y_{0k})\sin\phi']^2}{r'^2(1 - e'^2)} \\ -\dfrac{[-(x - x_{0k})\sin\phi' + (y - y_{0k})\cos\phi']^2}{r'^2} \end{array} \right\}, \tag{26}$$

where A' is the amplitude, r' the characteristic spatial scale, e' the eccentricity, and ϕ' the angle of the major axis with respect to the x axis. The upper- and lower-layer disturbances have initially the same amplitude but the lower disturbance is located downstream of the upper one to allow a substantial extraction of potential energy from the basic-state flow.

3. Baroclinic zonal flows with uniform horizontal shears

To simplify the problem, this section investigates the impact of uniform cyclonic and anticyclonic horizontal background shears onto the growth of lower-layer disturbances in presence of constant vertical background shears. To do so, the basic-state vorticity is defined as a constant in each layer over a large area centered in the middle of the domain (two-thirds of the domain). Because the model is biperiodic, the basic-state zonal wind must be periodic and the averaged basic-state vorticity must be zero. Therefore, outside the region of constant basic-state vorticity, the basic-state vorticity is defined using cosine profiles in such a way that its spatial average is zero over the whole domain. In the present section, all the disturbances are initialized in the center of the domain in the region of constant basic-state vorticity and we have checked that disturbances stay in that region during the whole simulations.

Within the region of constant basic-state vorticity, the basic-state zonal wind profiles have the following expression:

$$\overline{u}_u = -\alpha c_u^x y + \alpha\lambda c^z, \tag{27}$$

$$\overline{u}_l = -\alpha c_l^x y, \tag{28}$$

where α corresponds to a standard shear value (see Table 1). The c_k^x for $k \in [u, l]$ and c^z correspond to nondimensional parameters determining respectively the horizontal shear in each layer k and the vertical shear. Note that $\alpha c^z = (f/N)(\partial u/\partial z)$ is an estimate of the baroclinicity (i.e., the Eady parameter divided by 0.31)

and more precisely the maximum of the baroclinic generation rate CB/($K' + P'$) (Rivière et al. 2004; Gilet et al. 2009). The αc_k^x for $k \in [u, l]$ is an estimate of the horizontal deformation in each layer k and more precisely the maximum of the barotropic generation rate $\mathbf{E}_k \cdot \mathbf{D}_k / (K' + P')$. If $c^z = c_l^x = c_u^x$, means that the maxima of the barotropic and baroclinic generation rates are equal.

In presence of uniform shears, $F^{\text{lin}} = F_0^{\text{lin}} + F_\beta^{\text{lin}}$ depends on the following expressions:

$$F_0^{\text{lin}} = -\lambda^{-2}[\lambda\alpha c^z \Delta(v_u' + v_l') - \alpha(c_u^x - c_l^x) y \Delta(v_u' + v_l') + 2\alpha c_l^x \partial_y v_u' - 2\alpha c_u^x \partial_y v_l'], \tag{29}$$

$$F_\beta^{\text{lin}} = -\lambda^{-2}\beta(v_u' - v_l'). \tag{30}$$

All the terms in the previous two equations are controlled by the basic-state parameters c^z, c_l^x, c_u^x, and β. Note finally that because uniform shears are considered in this section, basic-state relative vorticity gradients are zero and the effective beta is reduced to β [see second term on the rhs of Eq. (8)]. The value of β is therefore artificially increased beyond its usual value in midlatitudes to reproduce the stronger effective beta in presence of localized jets.

a. *Vertical velocity induced by the various basic-state parameters*

1) THE EFFECT OF THE BASIC-STATE VERTICAL SHEAR AND PV GRADIENT

Let us first analyze the case without horizontal shears ($c_u^x = c_l^x = 0$) with a positive vertical shear $c^z > 0$. Figure 1a shows the vertical velocity due to the part of the linear term depending on the upper disturbance—that is, F_0^{lin} when v_l' equals 0, which can be reduced to $F_0^{\text{lin}}(v_l' = 0) = -\lambda^{-1}\alpha c^z \Delta v_u'$. It shows that there is ascending and descending motion respectively downstream and upstream of a cyclone when the vertical shear c^z is positive. Because the upper disturbance is located upstream of the lower one, its velocity induces ascending motions above the lower disturbance that will tend to intensify it. This intensification is commonly explained by noting that the perturbation relative vorticity will increase via the stretching term $f_0 \partial\omega/\partial p$ but this can be viewed from a kinetic energy perspective. The lower-layer kinetic energy evolution [Eq. (19)] depends on the sum CV + CI/2 = $\lambda^{-1} s \omega_{u-l}' \psi_l'$, which is mainly positive because the part of $\lambda^{-1} s \omega_{u-l}' \psi_l'$ related to the upper disturbance is mainly negative above the minimum streamfunction at the lower layer. In other words, when there is a dominant westward tilt with height of the perturbation streamfunction isolines with a phase tilt of 90° as in the present case, v_u' is well anticorrelated with ψ_l' leading to a strong correlation between $\lambda^{-1} s \omega_{u-l}^{\text{lin}}(v_l' = 0)$ and to large positive values of CV + CI/2. On the contrary, the vertical velocity due to the part of the linear term depending on the lower disturbance $F_0^{\text{lin}}(v_u' = 0) = -\lambda^{-1}\alpha c^z \Delta v_l'$ (Fig. 1b) is in quadrature phase with ψ_l' and thus does not modify the lower-layer kinetic energy.

As already discussed in section 2b, we expect that the β term tends to diminish the relative vorticity growth of the lower-layer perturbation. The stabilizing effect of β in the lower layer can be also viewed in terms of kinetic energy because F_β^{lin} (Fig. 1d) is mainly negative in the region where the lower-layer streamfunction is negative. The β term thus creates descending motions above the lower-layer perturbation that tends to diminish the kinetic energy growth due to F_0^{lin} (Fig. 1c).

The **Q** vector due to the nonlinear term (arrows in Fig. 1e) is strong and poleward oriented in the region located between the two cyclonic disturbances because $Q_y^{\text{nl}} \simeq -0.5\lambda^{-1} s \partial_y (u_u' + u_l')(v_u' - v_l')$ is positive in that region since $(v_u' - v_l') > 0$ and $\partial_y (u_u' + u_l') < 0$. This creates ascending motions to the north and descending motions to the south of the disturbances; but $\lambda^{-1} s \omega_{u-l}'$ due to the nonlinear term and ψ_l' are in quadrature phase and there is no global kinetic energy change coming from this term in that particular case.

In the end, the forcing induced by β can almost nullify the projection of the stretching term $\lambda^{-1} s \omega_{u-l}'$ onto ψ_l' created by the linear forcing F_0^{lin}, which would otherwise lead to kinetic energy growth in the lower layer.

2) THE EFFECT OF THE BASIC-STATE HORIZONTAL SHEARS

Without horizontal shears, the **Q** vector due to the linear part [Eq. (6)]—that is, $\mathbf{Q}^{\text{lin}}$—is eastward oriented along the segment line joining the two centers of the cyclones (see Fig. 1a). In presence of a cyclonic barotropic shear ($c_u^x = 1.0$, $c_l^x = 1.0$), $\mathbf{Q}^{\text{lin}}$ will have a strong poleward component in that region between the two disturbances. Indeed, $Q_y^{\text{lin}} \simeq -\lambda^{-1} s (1/2)(v_u' - v_l')(\partial/\partial y)(\overline{u}_u + \overline{u}_l) = \lambda^{-1} s (1/2)(v_u' - v_l')\alpha(c_u^x + c_l^x)$ is positive and maximum in the region where the dashed and solid black contours are superimposed upon each other (see Figs. 2a,b). Therefore, the convergence of the **Q** vector due to the presence of the upper disturbance $F_0^{\text{lin}}(v_l' = 0)$ will not reach its maximum in the region where the meridional velocity v_u' is maximum—that is, on the eastern side of the upper disturbance as in the case without shear (Fig. 1a)—but rather on its northeastern side (Fig. 2a). This can be also seen by considering Eq. (29) for $v_l' = 0$, that is, $F_0^{\text{lin}}(v_l' = 0) = -\lambda^{-1}\alpha c^z \Delta v_u' - 2\lambda^{-2}\alpha c_l^x \partial_y v_u'$. The second term on the rhs of the previous expression

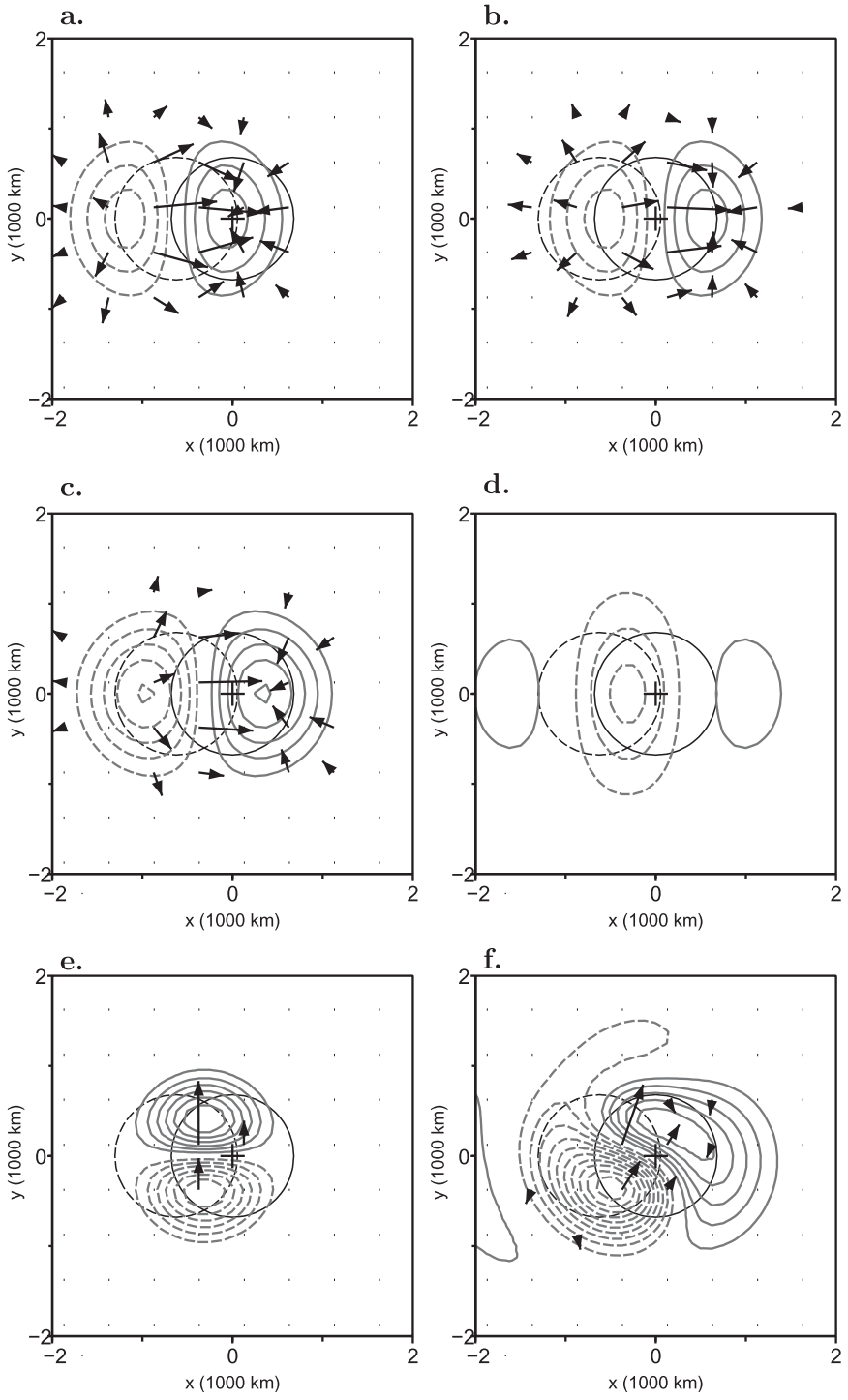

FIG. 1. Stretching term $-\lambda^{-1}s\omega'_{u-l}$, proportional to the vertical velocity at the interface between the two layers [gray contours; solid and dashed lines for ascending and descending motions, respectively; contour interval 5×10^{-11} s^{-2}] induced by (a) the linear term without β due to the presence of the upper disturbance [$F_0^{\text{lin}}(v'_l = 0)$], (b) the linear term without β due to the presence of the lower disturbance [$F_0^{\text{lin}}(v'_u = 0)$], (c) the linear term without β [sum of (a) and (b)], (d) the β term F_β^{lin}, (e) the nonlinear term F^{nl}, and (f) the sum of all the terms $F = F_0^{\text{lin}}(v'_l = 0) + F_0^{\text{lin}}(v'_u = 0) + F_\beta^{\text{lin}} + F^{\text{nl}}$. Arrows represent the **Q** vector for the different terms. The black dashed and solid contours represent respectively the perturbation streamfunction at the upper and lower layer (contour interval 10^7 m^2 s^{-1}, negative values only). The cross corresponds to the position of the minimum perturbation streamfunction at the lower layer.

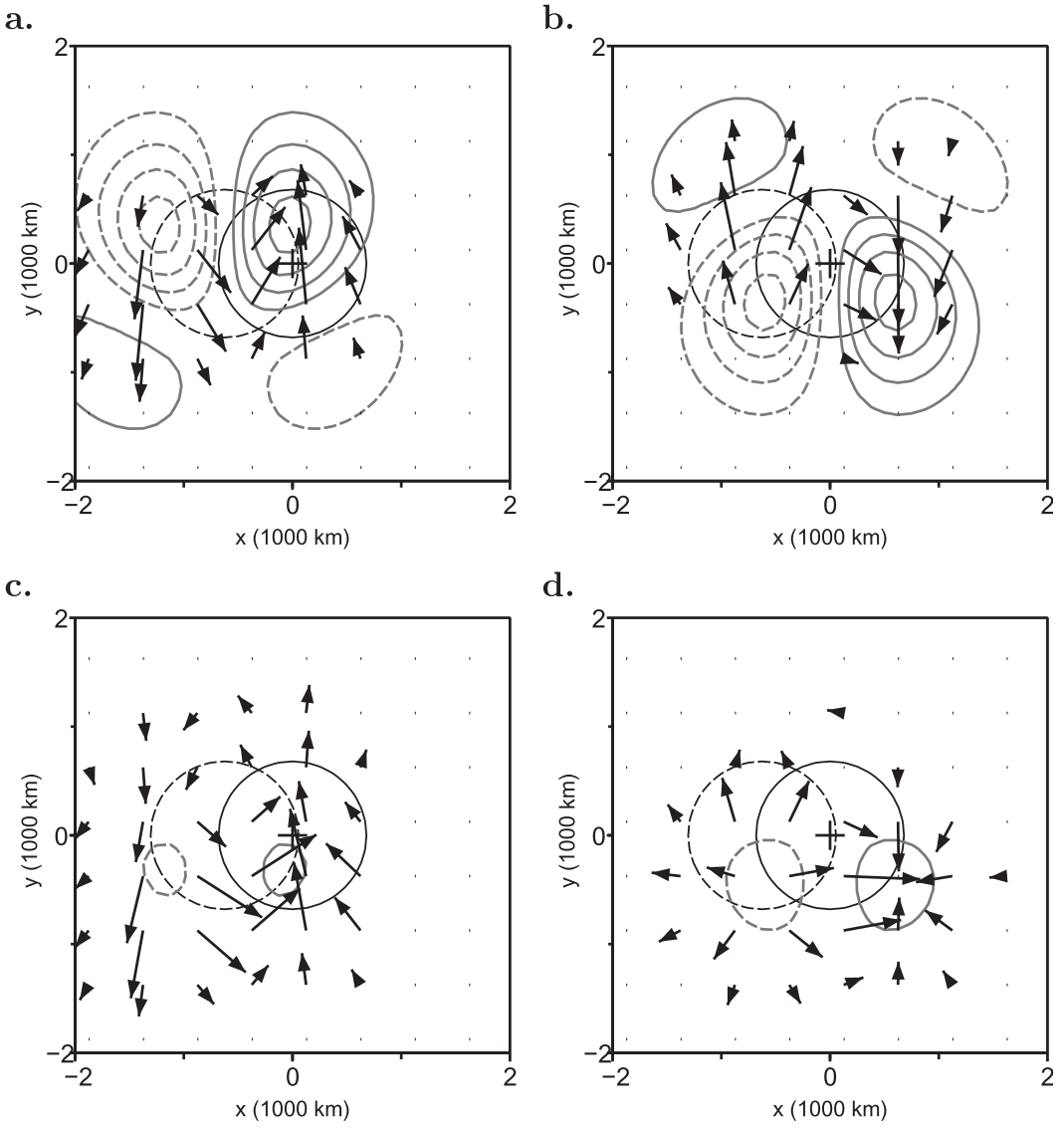

FIG. 2. Stretching term $-\lambda^{-1}s\omega'_{u-l}$ in the case of (a),(b) $c_u^x = 1.0$ and $c_l^x = 1.0$ and (c),(d) $c_u^x = 1.0$, $c_l^x = 0.0$ induced by (a),(c) the linear term without β due to the presence of the upper disturbance only $[F^{\text{lin}}(v'_l = 0)]$ and (b),(d) the linear term without β due to the presence of the lower disturbance only $[F^{\text{lin}}(v'_u = 0)]$. Arrows and contours as in Fig. 1.

is positive on the northeastern side of the upper disturbance. It means that the optimal growth for the lower-layer kinetic energy is no longer a pure westward tilt with height but rather a southwestward tilt with height. Figure 2b shows the vertical velocity forcing due to the lower disturbance. Since $F_0^{\text{lin}}(v'_u = 0) = -\lambda^{-1}\alpha c^z \Delta v'_l + 2\lambda^{-2}\alpha c_u^x \partial_y v'_l$, the vertical velocities are displaced southward relative to its no-shear counterpart (Fig. 1b).

Figures 2c and 2d show the effect of an upper-layer cyclonic shear without shear at the lower layer ($c_l^x = 0$). Since $F_0^{\text{lin}}(v'_l = 0) = -\lambda^{-2}(\lambda\alpha c^z \Delta v'_u - \alpha c_u^x y \Delta v'_u)$, the upper-layer shear effect due to the upper-layer cyclone is a southward shift of the vertical velocities because of stronger vertical shear to the south, which is confirmed by Fig. 2c. It is interesting to note that the upper-layer shear has the opposite effect to the barotropic shear in terms of the vertical velocity forcings induced by the upper-layer disturbance (cf. Figs. 2a and 2c). On the contrary, the vertical velocity forcings induced by the lower-layer disturbance are both displaced southward by increasing the barotropic shear (Fig. 2b) and the upper-layer shear (Fig. 2d). However, these vertical velocities induced by ψ'_l do not have any net effect on EKE because they are still in quadrature with ψ'_l.

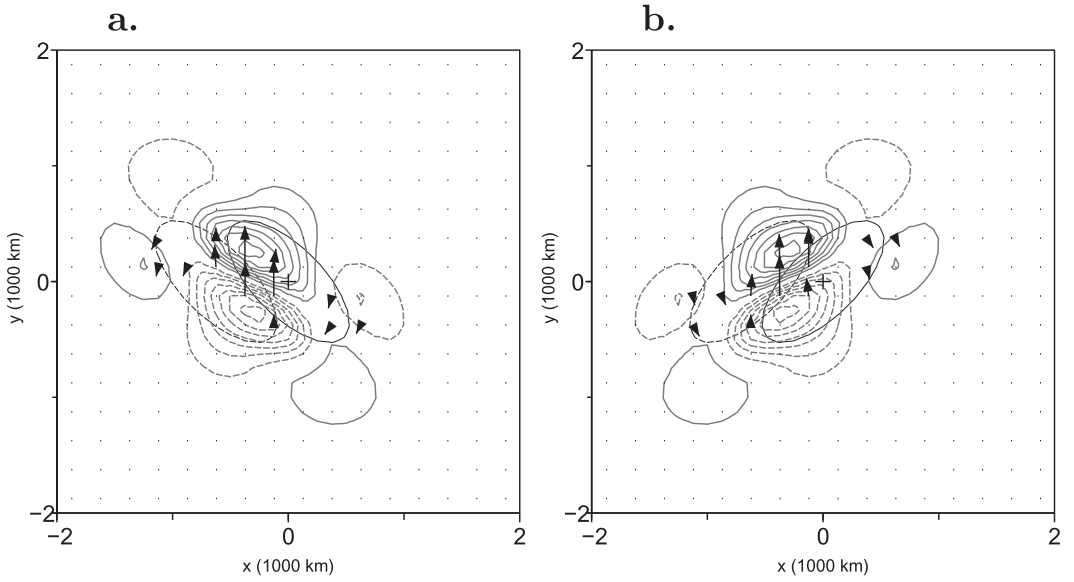

FIG. 3. Stretching term $-\lambda^{-1}s\omega'_{u-l}$ in the case of (a) $e' = 0.9$, $\phi' = \pi/4$ and (b) $e' = 0.9$, $\phi' = -\pi/4$ induced by the nonlinear term F^{nl}. Arrows and contours as in Fig. 1.

Let us summarize the direct effects of the horizontal shears in the linear part of the vertical velocities F_0^{lin} [Eq. (29)]. An increase in the upper-layer shear displaces the peak of ascending motions created by the upper cyclone to its southeastern side for the cyclonic shear and to its northeastern side for the anticyclonic shear. The converse occurs for an increase in the barotropic shear.

Another interesting aspect to consider is the nonlinear vertical velocity forcing when the disturbances are horizontally elongated as in Fig. 3. This effect can be an indirect effect of the horizontal shears. As in the no-elongation case (Fig. 1e), the **Q** vector is mainly poleward between the two disturbances because $\mathbf{Q}^{\mathrm{nl}} \simeq -\lambda^{-1}s[0, 0.5(v'_u - v'_l)\partial_y(u'_u + u'_l)]$. Thus, F^{nl} [see Eq. (9)] is mainly positive to the north and negative to the south and the stretching term has a south–north dipolar structure as in the no-elongation case (compare Figs. 3a,b to Fig. 1e). However, the forcing term $F^{\mathrm{nl}} \simeq \lambda^{-2}[\partial_y(v'_u - v'_l)\partial_y(u'_u + u'_l) + (v'_u - v'_l)\partial_y^2(u'_u + u'_l)]$ is no longer in quadrature with the lower-layer perturbation streamfunction ψ'_l as in the no-elongation case. Indeed, in the region where ψ'_l reaches its minimum, horizontal velocities (u'_l, v'_l) are close to zero. Furthermore, being close to its maximum in that region, its y derivative is close to zero and one can deduce that $F^{\mathrm{nl}} \simeq \lambda^{-2}(-\partial_y v'_l \partial_y u'_1 + v'_u \partial_y^2 u'_u)$. In the case of the cyclonic tilt (Fig. 3a), v'_u and u'_u have opposite signs and the product $v'_u \partial_y^2 u'_u$ is positive. Furthermore, $\partial_y v'_l > 0$ and $\partial_y u'_1 < 0$ leads to $-\partial_y v'_l \partial_y u'_1 > 0$. In the region where ψ'_l reaches its minimum, F^{nl} is therefore positive. This nonquadrature structure leads to a positive spatial average of the product between the nonlinear stretching term $\lambda^{-1}s\omega^{\mathrm{nl}}_{u-l}$ and the lower-layer perturbation streamfunction ψ'_l for the cyclonic tilt. A lower-layer kinetic energy increase (decrease) is then induced in the cyclonic (anticyclonic) orientation case. To conclude, even though the basic-state horizontal shear is not directly involved in the nonlinear stretching term, it may potentially have an impact on this term because it will tend to horizontally elongate the disturbances (cyclonically if the shear is cyclonic as in Fig. 3a and anticyclonically if the shear is anticyclonic as in Fig. 3b). We thus expect an increase and a decrease in the lower-layer kinetic energy due to the nonlinear term for the cyclonic and anticyclonic shear respectively.

b. Time evolution of the control simulations

The previous instantaneous diagnoses of the vertical velocities will be useful to analyze the time evolution of the disturbances in the following control simulations. The control simulations have the same vertical shear $c^z = 1.0$ and the same amplitude for the horizontal shears with $c_u^x = 1.0$ and $c_l^x = 0.5$ for the cyclonic-shear case and $c_u^x = -1.0$ and $c_l^x = -0.5$ for the anticyclonic-shear case. The lower-layer shear is weaker than the upper-layer one to reproduce the configuration of real midlatitude jets. The perturbation parameters are $A' = 18 \times 10^6\,\mathrm{m^2\,s^{-1}}$ and $r' = 9 \times 10^5\,\mathrm{m}$. The two columns on the left side of Fig. 4 correspond to the control simulations with anticyclonic and cyclonic shear without β and the other two on the right side to simulations with β. Let us first analyze the anticyclonic case without β (first

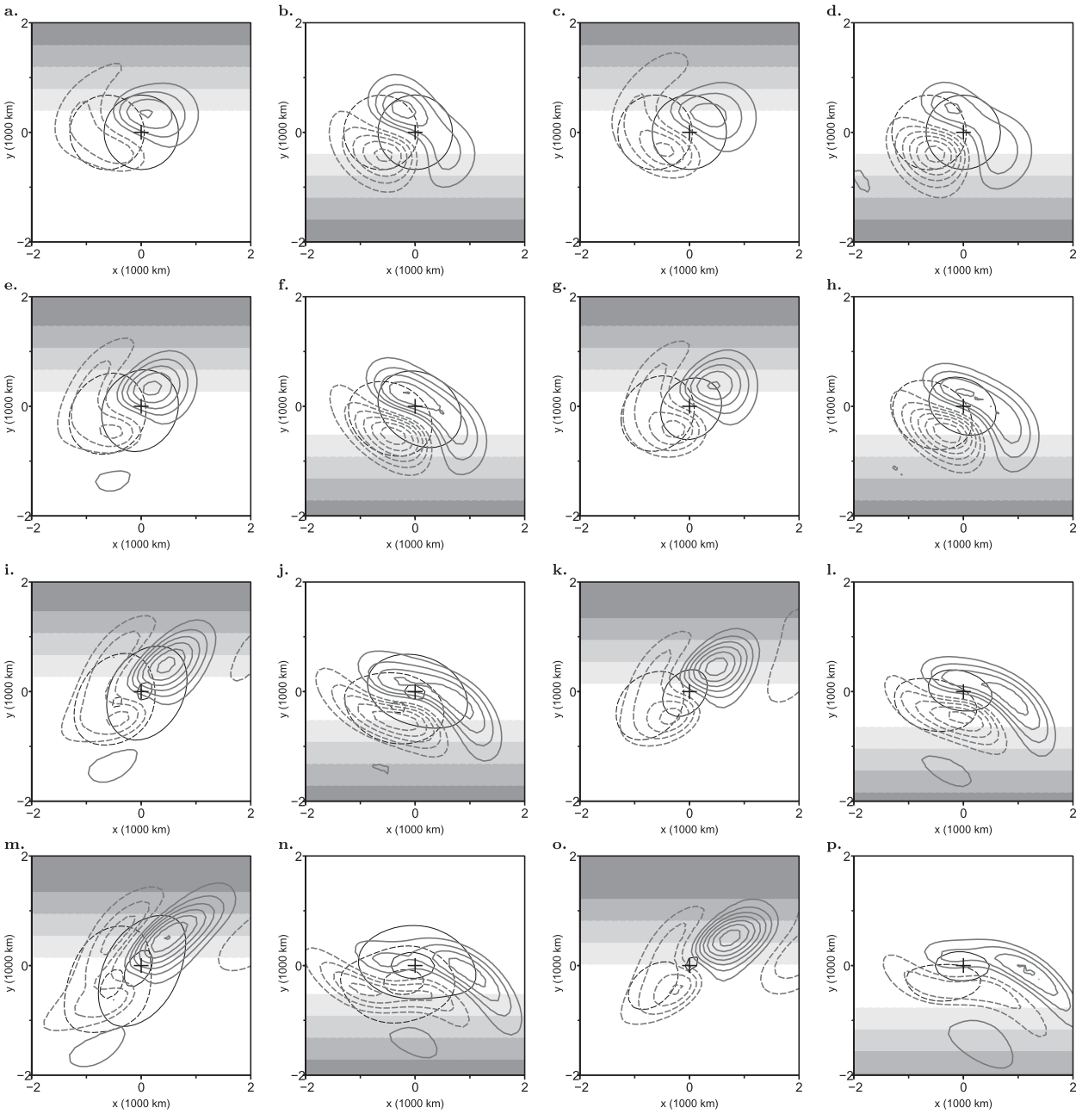

FIG. 4. Time evolution of the perturbation streamfunction at the lower (black solid contours) and upper (black dashed contours) layer and the stretching term $-\lambda^{-1}s\omega'_{u-l}$ (gray contours) for (first column) an anticyclonic shear ($c^z = 1.0$, $c_u^x = 1.0$, $c_u^x = -0.5$) without β, (second column) a cyclonic shear ($c^z = 1.0$, $c_u^x = -1.0$, $c_u^x = -0.5$) without β, (third column) an anticyclonic shear ($c^z = 1.0$, $c_u^x = 1.0$, $c_u^x = 0.5$) with $\beta = 3\beta_0$, and (fourth column) a cyclonic shear ($c^z = 1.0$, $c_u^x = 1.0$, $c_u^x = 0.5$) with $\beta = 3\beta_0$. Shadings correspond to the basic-state zonal wind in the lower layer (positive values only). The different times (top to bottom) are $t = 0.125$, $t = 6$, $t = 12$, and $t = 18$ h. Intervals as in Figs. 1 and 2.

column). As shown in Gilet et al. (2009), for the anticyclonic shear, both disturbances are stretched along the southwest–northeast direction and the lower disturbance keeps maintaining its position to the east of the upper disturbance (see Fig. 4m). This three-dimensional structure has some consequences from an energetic point of view as shown by averaging the various kinetic energy conversion rates over an area S spanning over the lower-layer perturbation streamfunction (hereafter denoted as $\langle\cdot\rangle_S$). Because of the stretching of the

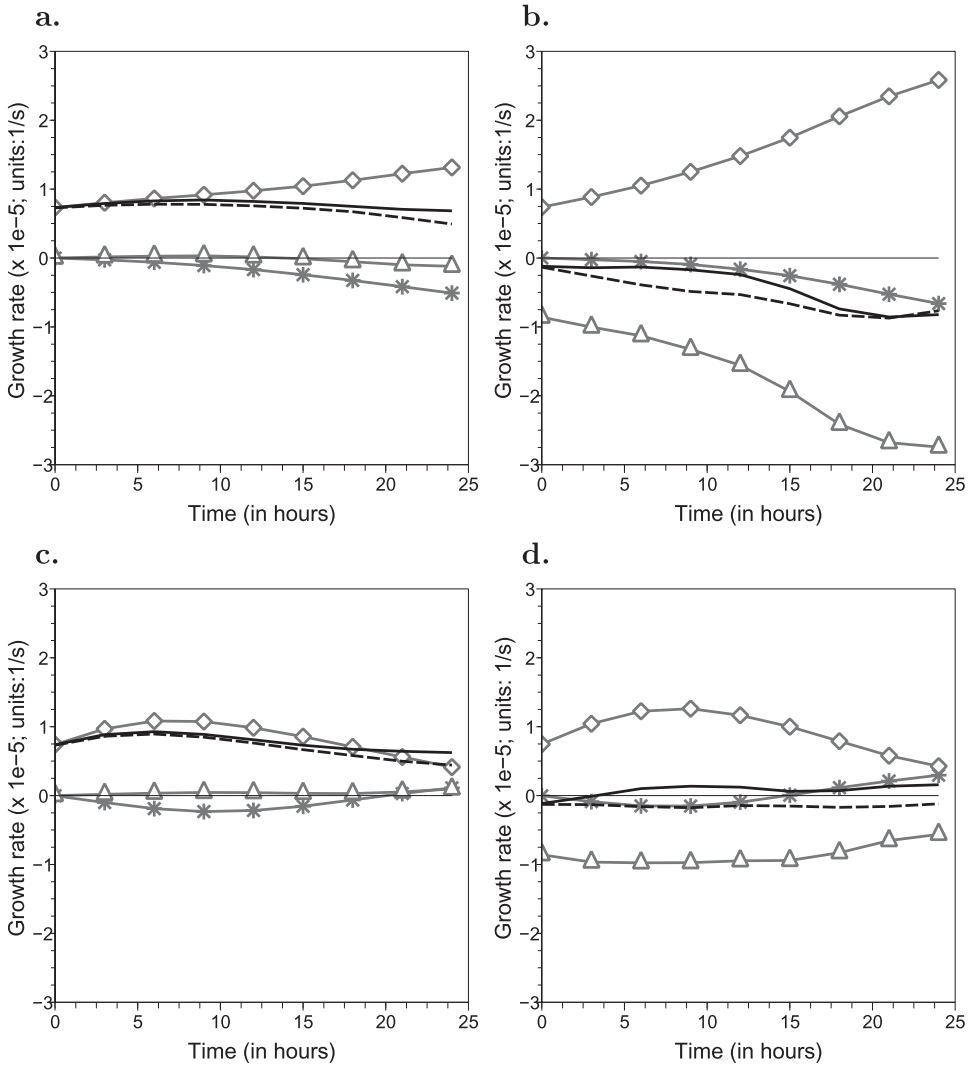

FIG. 5. Time evolution of the lower-layer EKE growth rate $(1/\langle K_l' \rangle_S)(d\langle K_l' \rangle_S/dt)$(dashed black lines) for disturbances embedded in (a),(b) an anticyclonic shear ($c^z = 1.0$, $c_u^x = -1.0$, $c_u^x = -0.5$) and (c),(d) a cyclonic shear ($c^z = 1.0$, $c_u^x = 1.0$, $c_u^x = 0.5$). Cases are for (left) $\beta = 0$ and (right) $\beta = 3\beta_0$. The gray lines with triangles, diamonds, and stars and the solid black line correspond respectively to $\langle \mathrm{CV} \rangle_S/\langle K_l' \rangle_S$, $\langle \mathrm{CI}/2 \rangle_S/\langle K_l' \rangle_S$, $\langle \mathbf{E}_l \cdot \mathbf{D}_l \rangle_S/\langle K_l' \rangle_S$, and the sum of all three terms. Spatial averages $\langle \cdot \rangle_S$ are made locally over a square S with half-length 2000 km and centered on the minimum perturbation streamfunction at the lower layer at each time. Abscissas are in hours.

perturbation along the dilatation axes, the barotropic conversion rate $\langle \mathbf{E}_l \cdot \mathbf{D}_l \rangle_S/\langle K_l' \rangle_S$ is negative (gray line with stars in Fig. 5a) and the perturbation is losing energy via barotropic interaction. However, because of the maintained westward tilt with height of the perturbation streamfunction, $\langle \mathrm{CI}/2 \rangle_S/\langle K_l' \rangle_S$ (gray line with diamonds in Fig. 5a) is positive [cf. section 3a(1)] and even increases during the simulation. The convergence of the vertical ageostrophic fluxes $\langle \mathrm{CV} \rangle_S/\langle K_l' \rangle_S$ is close to zero (gray line with triangles in Fig. 5a). This can be easily explained by noting that the dominant term of F_0^{lin} [Eq. (29)] is $-\lambda^{-1}\alpha c^z \Delta(v_u' + v_l')$, which is in quadrature phase with $\psi_u' + \psi_l'$. This renders the product between $\lambda^{-1} s \omega_{u-l}'$ and $\psi_u' + \psi_l'$, that is, CV [Eq. (23)], small on average. To conclude the discussion of this simulation, since $\langle \mathrm{CV} \rangle_S/\langle K_l' \rangle_S$ is mostly zero and $\langle \mathrm{CI}/2 \rangle_S/\langle K_l' \rangle_S$ is positive with stronger amplitude than the negative values of $\langle \mathbf{E}_l \cdot \mathbf{D}_l \rangle_S/\langle K_l' \rangle_S$, the sum of the three terms during the whole simulation (solid black lines in Fig. 5a) is positive and close to the kinetic energy

local growth rate (dashed black lines in Fig. 5a). The difference between the two curves is due to the horizontal redistribution terms [see Eq. (16)], which are not exactly zero when the spatial average is locally computed.

The anticyclonic case with β (third column of Fig. 4) exhibits similar behavior but the amplitudes of the upper and lower disturbances are significantly reduced compared to the case without β (first column of Fig. 4). This is consistent with the well-known stabilizing effect of β in baroclinic instability such as on normal modes (Vallis 2006) or singular modes (Rivière et al. 2001). Furthermore, the lower-layer streamfunction decreases more rapidly than the upper-layer one (see Fig. 4o). The kinetic energy budget in Fig. 5b shows that (gray line with triangles), which redistributes kinetic energy from lower to upper layer, is the prime driver of this growth difference. The value of $\langle \mathrm{CV} \rangle_S / \langle K_l' \rangle_S$ is so largely negative that the sum $(\langle \mathbf{E}_l \cdot \mathbf{D}_l \rangle_S + \langle \mathrm{CV} \rangle_S + \langle \mathrm{CI}/2 \rangle_S) / \langle K_l' \rangle_S$ is negative throughout the simulation.

In the cyclonic-shear case without and with β (second and fourth columns of Fig. 4), as shown in Gilet et al. (2009), the axes of the two cyclonic disturbances turn cyclonically and there is no elongation along the dilatation axes. It leads to smaller negative values for $\langle \mathbf{E}_l \cdot \mathbf{D}_l \rangle_S / \langle K_l' \rangle_S$ than in the anticyclonic cases and even slightly positive ones after 20 h (cf. the gray curves with stars between Figs. 5a and 5c and between Figs. 5b and 5d). The value of $\langle \mathrm{CI}/2 \rangle_S / \langle K_l' \rangle_S$ is strongly positive but decreases after a while without and with β (see the gray lines with diamonds in Figs. 5c,d). The quantity $\langle \mathrm{CV} \rangle_S / \langle K_l' \rangle_S$ is close to zero without β and is strongly negative with β but its amplitude decreases with time (see the gray lines with triangles in Figs. 5c,d). Indeed, as explained before in presence of β, CI and CV are initially quite large when the lower cyclone is downstream of the upper one but have opposite signs. Whereas this configuration is maintained in the anticyclonic shear, it is only transient in the cyclonic shear because the two disturbances turn around each other. This largely explains why the absolute amplitudes of both $\langle \mathrm{CI}/2 \rangle_S / \langle K_l' \rangle_S$ and $\langle \mathrm{CV} \rangle_S / \langle K_l' \rangle_S$ are relatively small and even decrease after 10 h in the cyclonic shear. Without β, there are not many differences between the EKE growth rates in both shears (cf. the black lines in Figs. 5a,c). However, with β, because CV becomes much more strongly negative in the anticyclonic shear than in the cyclonic shear (cf. the gray lines with triangles in Figs. 5b,d), the EKE growth rate is negative in the former shear and close to zero in the latter one (see the black lines in Figs. 5b,d).

Another large difference between the two shears concerns the eddy potential energy (EPE) budget (Fig. 6). Since the westward tilt with height is maintained with time in the anticyclonic shear, $\langle \mathrm{CB} \rangle_S / \langle P' \rangle_S$ is maintained with large positive values during the whole simulation (gray curves with squares in Figs. 6a,b). On the contrary, in the cyclonic-shear case, $\langle \mathrm{CB} \rangle_S / \langle P' \rangle_S$ decreases rapidly with time (gray curves with squares in Figs. 6c,d) because the westward tilt with height is not maintained. This difference explains why the EPE growth rate is much smaller in the cyclonic shear than in the anticyclonic shear. This result is valid with and without β even though we notice that the potential energy growth rates are smaller with β than without β. This last result is difficult to interpret because β does not appear in the expression of CB [see Eq. (24)].

Figure 7 details the budget of the sum of the internal conversion rate and the convergence of the vertical ageostrophic fluxes $\mathrm{CV} + \mathrm{CI}/2 = \lambda^{-1} s \omega_{u-l}' \psi_l'$ by analyzing the various terms involved in the stretching term $-\lambda^{-1} s \omega_{u-l}' \psi_l'$. During the anticyclonic-shear run, there is an increase with time in the difference between the cases without and with β (cf. the black lines in Figs. 7a,b) for $\langle \mathrm{CV} + \mathrm{CI}/2 \rangle_S / \langle K_l' \rangle_S$. On the contrary, during the cyclonic-shear run, there is a slight decrease with time in the difference between the cases without and with β (cf. the black lines in Figs. 7c,d). This can be explained in large part by the β term F_β^{lin} [Eq. (30)]. For the anticyclonic shear, $\langle \mathrm{CV}+\mathrm{CI}/2 \rangle_S / \langle K_l' \rangle_S$ due to F_β^{lin} (gray solid line in Fig. 7b) becomes more and more negative with time. This could be explained by the stretching of the cyclones, which are more and more meridionally tilted (see the third column of Fig. 4), increasing the ratio between the perturbation meridional and zonal velocities. The ratio $\langle \mathrm{CV}+\mathrm{CI}/2 \rangle_S / \langle K_l' \rangle_S$ could be thus more negative because of a greater ratio between meridional velocities and K_l'. For the cyclonic shear, $\langle \mathrm{CV}+\mathrm{CI}/2 \rangle_S / \langle K_l' \rangle_S$ due to F_β^{lin} (gray solid line in Fig. 7d) becomes less and less negative with time because the two disturbances are turning around each other without being significantly stretched. This makes the correlation between v_u' and ψ_l' small and the value of $\langle \mathrm{CV}+\mathrm{CI}/2 \rangle_S / \langle K_l' \rangle_S$ due to F_β^{lin} becomes less and less negative during the simulation. The linear part F_0^{lin} for the cyclonic shear becomes less positive in the case with β (gray dashed lines in Figs. 7c,d) while it does not change so much for the anticyclonic shear (gray dashed lines in Figs. 7a,b).

The nonlinear part of $\langle \mathrm{CV}+\mathrm{CI}/2 \rangle_S / \langle K_l' \rangle_S$ due to F^{nl} (dash-dotted lines in Fig. 7) participates in the difference between the anticyclonic-shear and cyclonic-shear cases. It is negative and positive in the anticyclonic-shear and cyclonic-shear case respectively as expected from Fig. 3. The presence of β amplifies this nonlinear effect (cf. Figs. 7a,b and Figs. 7c,d), which can be interpreted as follows. In the anticyclonic-shear case, cyclones are slightly less meridionally stretched and more southwest–northeast

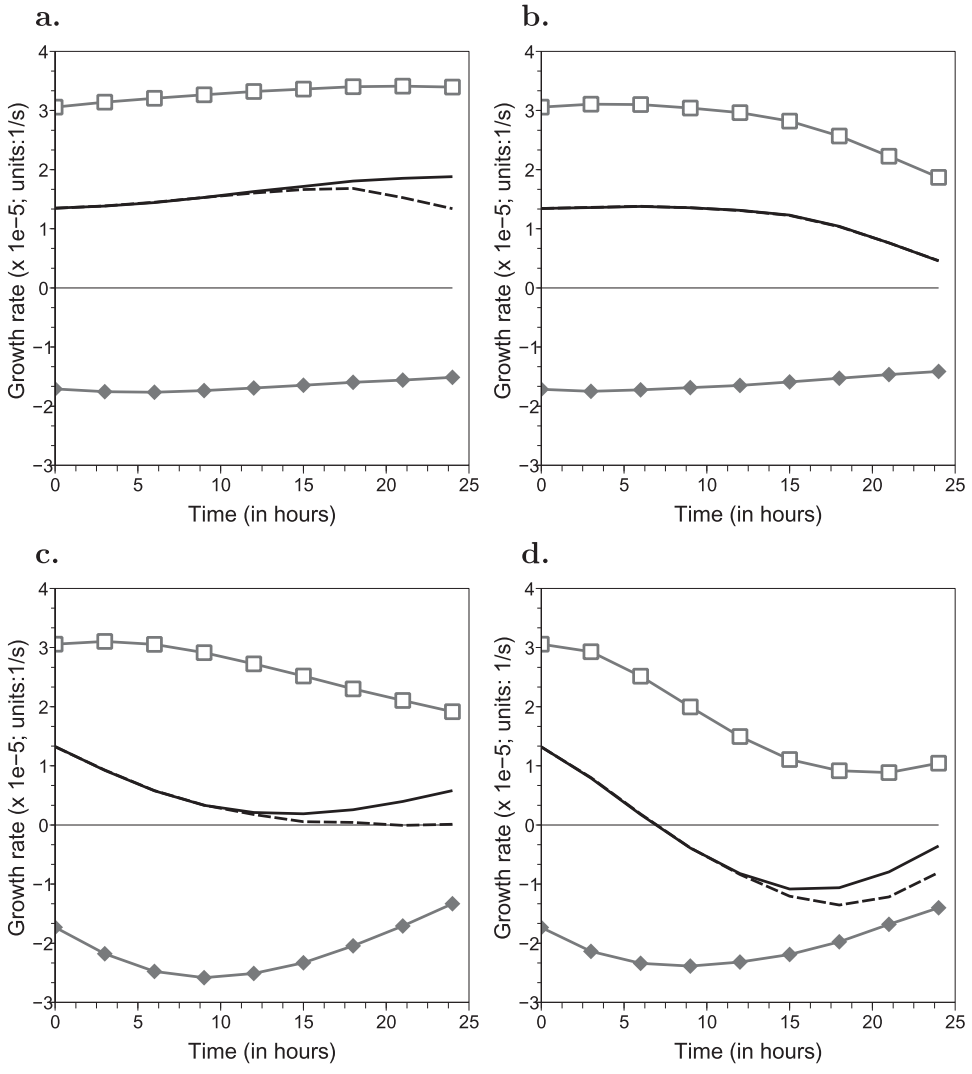

FIG. 6. Time evolution of the eddy potential energy (EPE) growth rate $(1/\langle P'\rangle_S)(d\langle P'\rangle_S/dt)$ (dashed black lines) for disturbances embedded in (a),(b) an anticyclonic shear ($c^z = 1.0$, $c_u^x = -1.0$, $c_u^x = -0.5$) and (c),(d) a cyclonic shear ($c^z = 1.0$, $c_u^x = 1.0$, $c_u^x = 0.5$). Cases are for (left) $\beta = 0$ and (right) $\beta = 3\beta_0$. The gray lines with squares and diamonds, and the solid black lines correspond respectively to $\langle \mathrm{CB}\rangle_s/\langle P'\rangle_s$, $\langle 0 - \mathrm{CI}\rangle_s/\langle P'\rangle_s$, and the sum of these terms $\langle \mathrm{CB} - \mathrm{CI}\rangle_s/\langle P'\rangle_s$. Spatial averages $\langle\cdot\rangle_S$ are made locally over a square S with half-length 2000 km and centered on the minimum perturbation streamfunction at the lower layer at each time. Abscissas are in hours.

oriented with β than without β. This leads to a more negative value of CV + CI/2 due to F^{nl} with β. In the cyclonic-shear case, cyclones less rapidly rotate cyclonically with β and therefore stay a longer time with a northwest–southeast elongation. The effect is to increase the positive value of CV + CI/2 due to F^{nl}. This might explain part of the amplifying difference between the cyclonic and anticyclonic shear cases in the presence of β.

To conclude, the stabilizing effect of β is less efficient in the cyclonic-shear case than in the anticyclonic-shear case as the lower-layer kinetic energy growth rate is greater in the former case than in the latter in presence of β while the two growth rates have equivalent amplitudes when β is zero. This is explained in large part by the direct effect of β in the vertical velocity forcing (F_β^{lin}) as well as by the indirect effect in the nonlinear vertical velocity forcing (F^{nl}), which are both involved in the sum CV + CI/2.

c. *Sensitivity to various parameters*

The previous control simulations were obtained for specific values of the parameters. The purpose of the present section is to change the value of each parameter to identify its role in the difference between

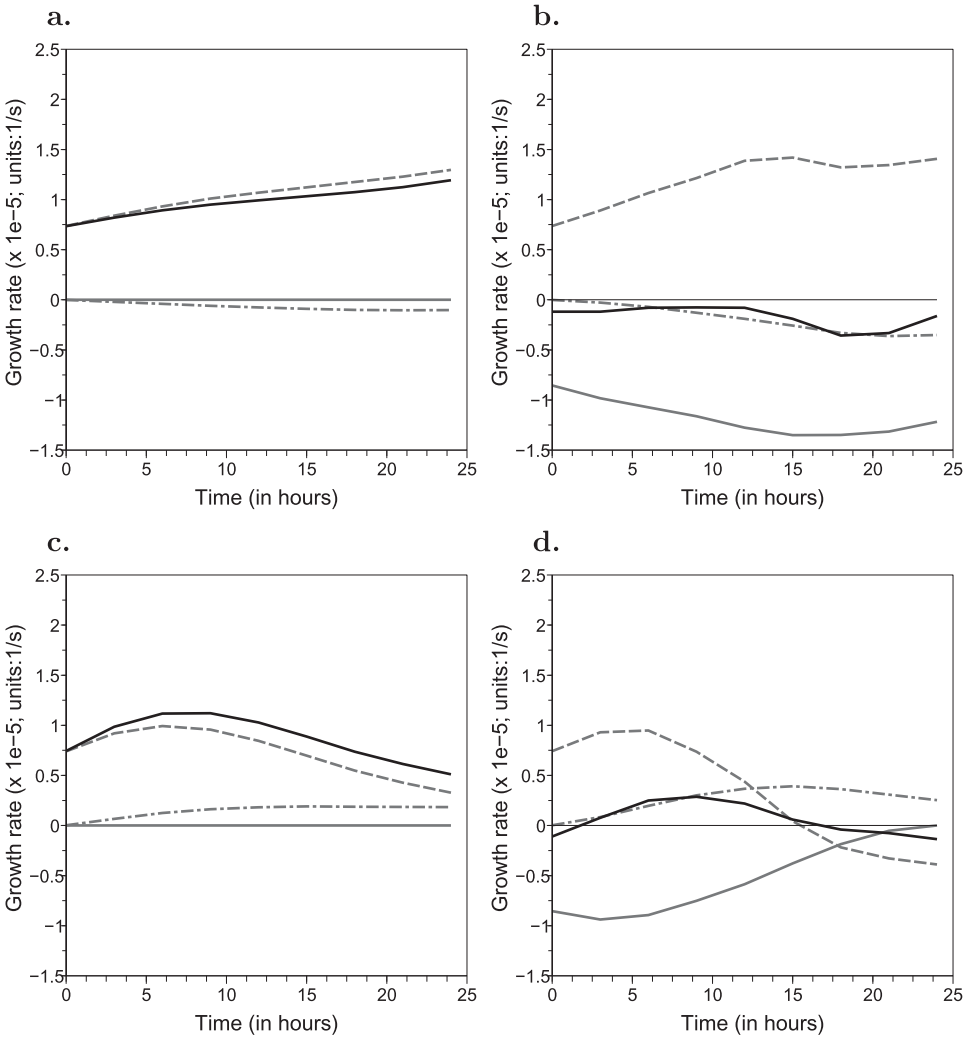

FIG. 7. Time evolution of the sum of the internal conversion rate and the convergence of the vertical ageostrophic fluxes $\langle \mathrm{CV}+\mathrm{CI}/2\rangle_s/\langle K_l'\rangle_S$ (black lines) at the lower layer for (a),(b) an anticyclonic shear ($c^z = 1.0$, $c_u^x = -1.0$, $c_u^x = -0.5$) and (c),(d) a cyclonic shear ($c^z = 1.0$, $c_u^x = 1.0$, $c_u^x = 0.5$). Cases are for (left) $\beta = 0$ and (right) $\beta = 3\beta_0$. The dashed, solid, and dash-dotted gray lines correspond respectively to the part of $\langle \mathrm{CV}+\mathrm{CI}/2\rangle_s/\langle K_l'\rangle_S$ coming from the linear terms without β F_0^{lin} and with β F_β^{lin} and the nonlinear term (F^{nl}). Spatial averages $\langle\cdot\rangle_S$ are as in Fig. 5.

cyclonic- and anticyclonic-shear cases. Figure 8 shows the sensitivity of the EKE amplification between $t = 0$ and $t = 24$ h, $\langle K_l'\rangle_S(t = 24\,\mathrm{h})/\langle K_l'\rangle_S(t = 0\,\mathrm{h})$, to various parameters. Spatial averages are still computed over a square S whose center is the lower-layer perturbation streamfunction minimum. When spatial averages are made over the whole domain amplification rates are greater than when they are made over the area S because energy redistribution terms [second term on the rhs of Eq. (5)] tend to disperse energy outside the region where finite-amplitude disturbances are. Note that this horizontal dispersion of energy is even stronger when β is present (not shown) because of the so-called Rossby radiation of energy in the presence of the PV gradient (Oruba et al. 2013). Despite these distinct features between the global and local averages, the results below are valid for both averages and only local ones are shown in Fig. 8.

Generally speaking, the presence of β reduces EKE amplification rates (cf. the dashed and solid lines in Fig. 8). The stabilizing effect of β is more efficient in the anticyclonic-shear case than in the cyclonic-shear case and confirms the results found before.

Let us now look at the sensitivity to individual parameters. Since the difference between the two horizontal shears is a nonlinear phenomenon, it is natural to change the value of the initial amplitude of the disturbances. Figure 8a shows the sensitivity to the perturbation

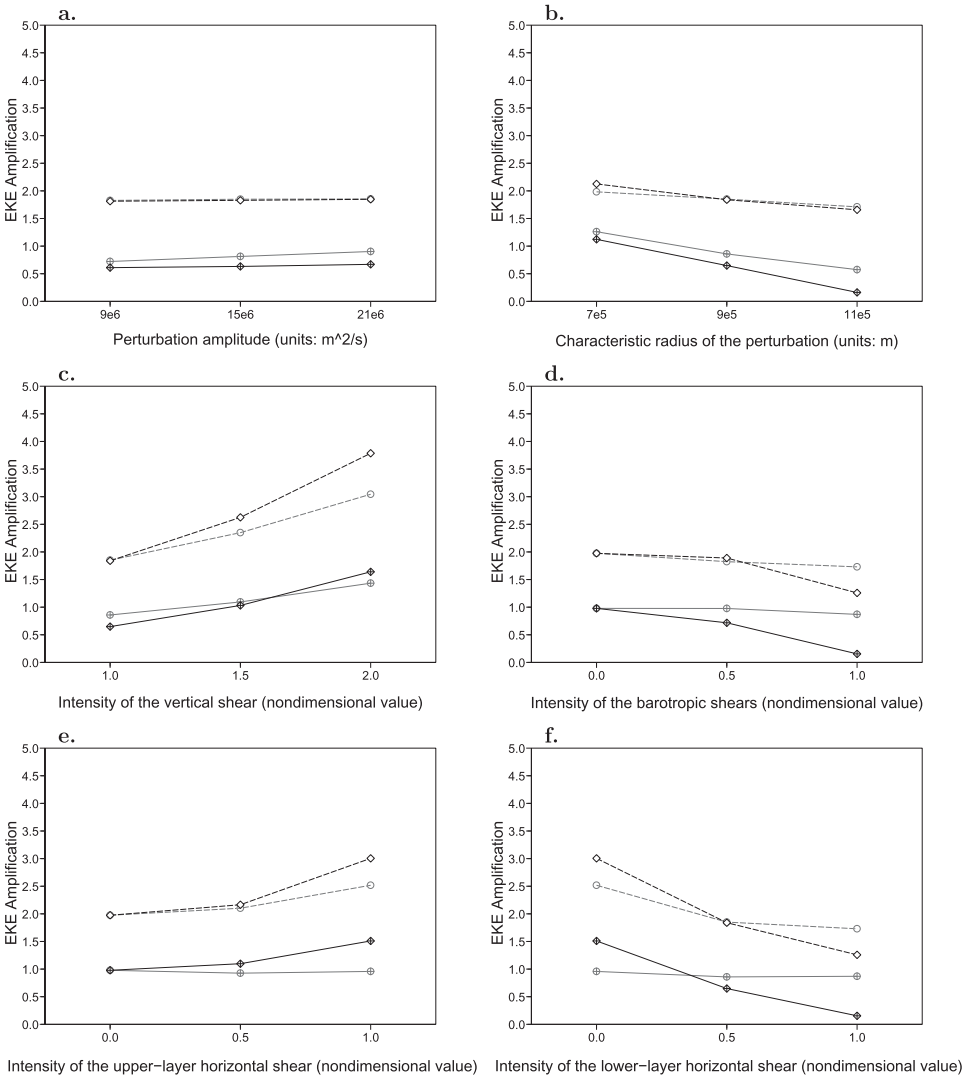

FIG. 8. Lower-layer kinetic energy amplification between $t = 0$ and $t = 24$ h as function of (a) the initial amplitude of the disturbances A', (b) the perturbation radius r', (c) the basic-state vertical shear c^z, (d) the basic-state barotropic horizontal shear $|c_u^x| = |c_l^x|$, (e) the basic-state upper-layer horizontal shear $|c_u^x|$ for $c_l^x = 0$, and (f) the basic-state lower-layer horizontal shear $|c_l^x|$ for $|c_u^x| = 1.0$. The gray and black lines correspond respectively to the cyclonic- and anticyclonic-shear cases while the dashed and solid lines correspond to the cases with $\beta = 0$ and $\beta = 3\beta_0$. Kinetic energy spatial averages are made locally over the same square S centered on the minimum lower-layer perturbation streamfunction as in Figs. 5 and 7.

amplitude A'. In the case without β (dashed lines), changing the perturbation amplitude does not modify the result. In presence of β (solid lines), the EKE amplification is systematically larger for the cyclonic-shear case than the anticyclonic-shear case and the difference between the two cases slightly increases with the perturbation amplitude. The last result was expected because the two cases converge toward each other for very small disturbances.

Figure 8b shows the sensitivity to the horizontal scales of the disturbances r', keeping constant the distance between them. The two simulations without β are generally similar (dashed lines). With β, EKE amplification rates are stronger for smaller length scales. This result is consistent with the previous sensitivity test to A'. Indeed, the eddy vorticity simply scaling as A'/r'^2, an increase in A' would have the same effect on vorticity amplitude as a decrease in r'^2. For all the length scales in presence of β, the growth rates are greater in the cyclonic-shear case than in the anticyclonic-shear case and the difference between the two cases slightly increases by increasing the length scale. This last result cannot be

simply explained in terms of vorticity amplitude because an increase in r' (which decreases the vorticity amplitude) leads to larger differences between the cyclonic and anticyclonic-shear cases similarly to an increase in A' (which increases the vorticity amplitude).

The sensitivity to the basic-state vertical shear c^z is shown in Fig. 8c. As expected, all growth rates become larger by increasing c^z because CI becomes larger. In the case without β (dashed lines), the EKE amplification rate becomes larger for the anticyclonic shear than for the cyclonic shear for $c^z \geq 1.5$. With β (solid lines), the same thing occurs for $c^z \geq 2.0$. This is consistent with the fact that the westward tilt with height is maintained with time in the anticyclonic shear while it is not in the cyclonic shear. Indeed, following Eqs. (4) and (29), the term involving the vertical shear in CV + CI/2 can be expressed as $\mathrm{CV} + \mathrm{CI}/2 = -\lambda^{-1}\alpha c^z \psi_l'(\Delta - 2\lambda^{-2})^{-1}\Delta(v_u' + v_l')$, which is close to $-\lambda^{-1}\alpha c^z \psi_l' v_u'$ where ψ_l' is minimum. For the anticyclonic shear, since the westward tilt with height is well maintained, v_u' and ψ_l' are strongly anticorrelated and an increased c^z leads to a rapid increase in $-\lambda^{-1}\alpha c^z \psi_l' v_u'$ and thus in CV + CI/2. On the contrary, for the cyclonic shear, because v_u' and ψ_l' are not well anticorrelated, $\mathrm{CV} + \mathrm{CI}/2 \simeq -\lambda^{-1}\alpha c^z \psi_l' v_u'$ increases less rapidly with c^z. The same reasoning holds when looking at the vertical velocity forcing term involving β in Eq. (2.2), whose effects in CV + CI/2 can be written as $-\lambda^{-2}\beta\psi_l'(\Delta - 2\lambda^{-2})^{-1}(v_u' - v_l')$, which is also highly dependent on the correlation between v_u' and ψ_l'. However, c^z and β have opposite effects. The term involving c^z increases EKE while the one involving β decreases it. The c^z increase leads to a more rapid EKE increase in the anticyclonic shear than in the cyclonic shear while the β increase leads to a more rapid EKE decrease in the former shear than in the latter.

Figure 8d shows the sensitivity to the barotropic shear, that is when c_l^x and c_u^x are changed but maintained equal to each other. While the EKE amplification does not change much in the cyclonic shear, a strong barotropic shear practically eradicates any lower-layer cyclogenesis in the anticyclonic shear, especially in the case with β (black solid line). This can be explained in large part by the barotropic conversion rate. For large horizontal shears, the lower-layer cyclone embedded in the anticyclonic shear is strongly stretched leading to negative kinetic energy growth rates because of negative barotropic conversion rates. In the cyclonic shear, the lower-layer cyclone is not that stretched and its axis is not maintained along the dilatation axes: the barotropic conversion rate is thus relatively small. The quantity CV + CI/2 (not shown) is also responsible for the stabilizing effect of the barotropic anticyclonic shear. When this shear is increased, the nonlinear part of the vertical velocity leads to more and more negative tendencies which significantly reduces CV + CI/2. Differences in the nonlinear term are even larger in presence of β (not shown). It is consistent with Fig. 7 showing larger magnitudes of the nonlinear terms in presence of β (cf. the dash-dotted lines in Figs. 7a,b).

Figure 8e shows the sensitivity to the upper-layer shear c_u^x for $c_l^x = 0$. Since the lower-layer shear is zero, there is no barotropic sink and EKE amplification rates are greater than in the case with barotropic shear. The anticyclonic shear exhibits even stronger EKE amplification rates with increasing the upper-layer shear. This is mainly due to the linear part of the vertical velocity (not shown). As shown in Fig. 2c, the ascending motions due to the presence of the upper-layer cyclone are to the southeast for the cyclonic shear and to the northeast for the anticyclonic shear. Since the lower-layer cyclone is maintained to the northeast of the upper-layer cyclone in the anticyclonic shear (see the first and third columns in Fig. 4), there is a good correlation between the linear vertical velocity triggered by the upper-layer cyclone and the lower-layer streamfunction. Another effect that renders the previous correlation strong is due to the horizontal stretching of the disturbances that increases the ratio between the eddy meridional velocity and the eddy kinetic energy. Since $F_0^{\mathrm{lin}}(v_l' = 0) = -\lambda^{-2}(\lambda\alpha c^z \Delta v_u' - \alpha c_u^x y \Delta v_u')$, the associated linear stretching term $-\lambda^{-1} s\omega_{u-l}^{\mathrm{lin}}$ depends strongly on v_u'. Therefore, the ratio $\langle \mathrm{CV} + \mathrm{CI}/2\rangle / \langle K_l'\rangle_S$ depends on the ratio v_u'/K_l', which is greater for meridionally stretched cyclones. To conclude, the reinforcement of the upper-layer anticyclonic shear facilitates the EKE increase via the linear vertical velocity forcings.

Since Figs. 8d and 8e show that the increased barotropic and upper-layer shears respectively decrease and increase the EKE amplification rates in the anticyclonic-shear case, we expect a strong decrease in EKE amplification rates when the lower-layer shear is increased. This is precisely what Fig. 8f shows (see the black lines). The cyclonic-shear cases are less sensitive to the lower-layer shear (gray lines).

To conclude, increasing the basic-state vertical shear destabilizes the anticyclonic-shear cases more while increasing β or the lower-layer horizontal shear stabilizes them more than the cyclonic-shear ones. The sensitivity to perturbation parameters, such as to the spatial scale or the amplitude, shows less drastic differences between the two shears.

4. Meridionally confined zonal jet

In the present section, the jet-crossing phase undergone by a surface cyclone is investigated. To do so,

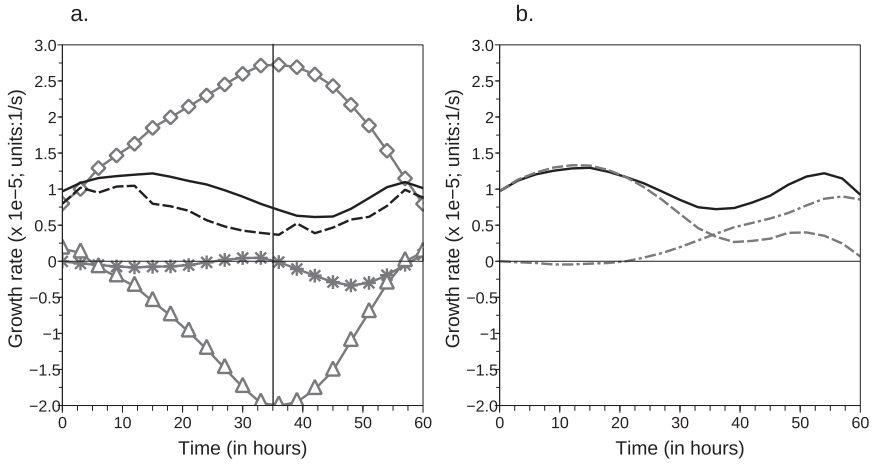

FIG. 9. The EKE budget at the lower layer in the simulation with disturbances embedded in a meridionally confined jet. (a) The time evolution of the kinetic energy growth rate $(1/\langle K_l' \rangle_S)(d\langle K_l' \rangle_S/dt)$ is shown by the dashed black line, the convergence of the vertical ageostrophic fluxes $\langle \mathrm{CV} \rangle_S/\langle K_l' \rangle_S$ by the gray line with triangles, the baroclinic internal conversion rate $\langle \mathrm{CI}/2 \rangle_S/\langle K_l' \rangle_S$ by the gray line with diamonds, the barotropic conversion term $\langle \mathbf{E}_l \cdot \mathbf{D}_l \rangle_S/\langle K_l' \rangle_S$ by the gray line with stars, and the sum of all three tendency terms by the solid black line. The vertical black line indicates the jet-crossing time. (b) The black line, the dashed gray line, and the dash-dotted gray lines correspond respectively to $\langle \mathrm{CV}+\mathrm{CI}/2 \rangle_S/\langle K_l' \rangle_S$, the part of $\langle \mathrm{CV}+\mathrm{CI}/2 \rangle_S/\langle K_l' \rangle_S$ due to the linear term (F^{lin}), and the part of $\langle \mathrm{CV}+\mathrm{CI}/2 \rangle_S/\langle K_l' \rangle_S$ due to the nonlinear term (F^{nl}). Spatial averages $\langle \cdot \rangle_S$ are made locally over a square S with half-length 1250 km and centered on the minimum perturbation streamfunction at the lower layer at each time.

a unique simulation is performed that is similar to the one described by Gilet et al. (2009). The initial conditions are the following: The basic-state flow consists of a meridionally confined zonal jet having a Gaussian horizontal profile with maximum wind speeds at the lower and upper layer equal respectively to 25 and 50 m s^{-1} [see the basic-state wind profile in Fig. 10 of Gilet et al. (2009)]. The perturbation flow is composed of the same two zonally aligned disturbances as in previous sections but localized to the south of the jet at a distance of 875 km. The distance between the two disturbances is 1000 km and other perturbation parameters are $A' = 2 \times 10^7$ m^2 s^{-1} and $r' = 1000$ km. As shown by Gilet et al. (2009), the two disturbances move northward through a generalized β-drift mechanism in presence of a positive barotropic PV gradient. The lower-layer cyclone crosses the jet axis around $t = 36$ h. Besides, during the evolution between $t = 0$ and $t = 60$ h, there exist two peaks in the EKE growth rate (see the dashed black line in Fig. 9a), one before the jet-crossing phase around $t = 12$ h and another at about $t = 60$ h. The average of the sum of the three terms $(\langle \mathbf{E}_l \cdot \mathbf{D}_l \rangle_S + \langle \mathrm{CV} \rangle_S + \langle \mathrm{CI}/2 \rangle_S)/\langle K_l' \rangle_S$ (solid black line in Fig. 9a) follows the same evolution as the EKE growth rate with the former being slightly greater than the latter because of horizontal energy outward flux at the boundary of the considered area. Note in particular that there exist also two peaks in $(\langle \mathbf{E}_l \cdot \mathbf{D}_l \rangle_S + \langle \mathrm{CV} \rangle_S + \langle \mathrm{CI}/2 \rangle_S)/\langle K_l' \rangle_S$ around $t = 12$ and $t = 60$ h. The barotropic conversion rate $\langle \mathbf{E}_l \cdot \mathbf{D}_l \rangle_S/\langle K_l' \rangle_S$ (gray line with stars in Fig. 9a) is mainly negative and its fluctuations play a minor role, albeit not negligible, in the evolution of $(\langle \mathbf{E}_l \cdot \mathbf{D}_l \rangle_S + \langle \mathrm{CV} \rangle_S + \langle \mathrm{CI}/2 \rangle_S)/\langle K_l' \rangle_S$. As the two disturbances get closer to the jet axis, because the vertical shear increases, $\langle \mathrm{CI}/2 \rangle_S/\langle K_l' \rangle_S$ (gray line with diamonds in Fig. 9a) is more and more positive and $\langle \mathrm{CV} \rangle_S/\langle K_l' \rangle_S$ (gray line with triangles in Fig. 9a) is more and more negative because of a stronger barotropic PV gradient close to the jet axis consistent with section 3. Note this evolution is also consistent with the uniform anticyclonic-shear case of Fig. 5b. On the contrary, once the disturbance is located on the cyclonic side, the amplitudes of $\langle \mathrm{CI}/2 \rangle_S/\langle K_l' \rangle_S$ and $\langle \mathrm{CV} \rangle_S/\langle K_l' \rangle_S$ decrease similarly to the uniform cyclonic-shear case of Fig. 5d. This is the sum of $\langle \mathrm{CV} + \mathrm{CI}/2 \rangle_S/\langle K_l' \rangle_S$ that explains the two growth stages, one on the anticyclonic side and the other on the cyclonic side, as shown by the similarity between $\langle \mathrm{CV} + \mathrm{CI}/2 \rangle_S/\langle K_l' \rangle_S$ (solid black line in Fig. 9b) and $\langle \mathbf{E}_l \cdot \mathbf{D}_l + \mathrm{CV} + \mathrm{CI}/2 \rangle_S/\langle K_l' \rangle_S$ (solid black line in Fig. 9a). However, the two peaks are related to different terms and mechanisms. During the first growth stage, the peak of $\langle \mathrm{CV} + \mathrm{CI}/2 \rangle_S/\langle K_l' \rangle_S$ is mainly due to the linear term F^{lin} (dashed curve in

Fig. 9b) while during the second growth stage, the peak of $\langle \mathrm{CV} + \mathrm{CI}/2 \rangle_S / \langle K_l' \rangle_S$ is mainly due to the nonlinear term F^{nl} (dash-dotted curve in Fig. 9b).

The snapshot of Fig. 10 at $t = 12$ h details the spatial structure of the various vertical velocity forcings (left column) and the corresponding CV + CI/2 (right column) during the first growth stage. At that time, the axis formed by the two disturbances is zonal. This renders the linear part of the stretching term $-\lambda^{-1} s \omega'_{u-l}$ well anticorrelated with the lower-layer perturbation streamfunction ψ'_l (Fig. 10a), leading to large positive values of CV + CI/2 coming from the linear term (Fig. 10b). To a lesser extent, the disturbances being also southwest–northeast tilted, the nonlinear part of the vertical velocity $-\lambda^{-1} s \omega'_{u-l}$ is very slightly correlated with the lower-layer perturbation streamfunction ψ'_l (Fig. 10c), which is similar to the case of Fig. 3b. It leads to negative values of CV + CI/2 above the minimum lower-layer perturbation streamfunction ψ'_l (Fig. 10d) but the local spatial average has only very weak negative values (see the dash-dotted line in Fig. 9b). The total CV + CI/2 is thus strongly positive because of the linear part of the vertical velocity.

At $t = 54$ h, the lower-layer perturbation is to the north-northeast of the upper-layer perturbation (see the dashed and solid black contours in the left column of Fig. 11). It implies a weak correlation between the linear part of the stretching term $-\lambda^{-1} s \omega'_{u-l}$ and the lower-layer perturbation streamfunction ψ'_l (Fig. 11a). However, the two disturbances are both slightly southeast–northwest horizontally tilted (see in particular the lower-layer perturbation in Fig. 11). Consistent with the case of Fig. 3a, this makes the nonlinear part of the stretching term $-\lambda^{-1} s \omega'_{u-l}$ positive close to the minimum of the lower-layer perturbation streamfunction (Fig. 11c). The nonlinear part of the stretching term $-\lambda^{-1} s \omega'_{u-l}$ and the lower-layer perturbation streamfunction are thus significantly anticorrelated. Consistent with this picture, the nonlinear part of CV + CI/2 (Fig. 11d) is positive when averaged around the lower-layer perturbation. Therefore, the total CV + CI/2 (Fig. 11f) during the second growth stage can be explained by the nonlinear part of CV + CI/2, which itself is mainly due to the three-dimensional structure of the disturbances characterized by a slight southeast–northwest tilt of the disturbances.

5. Conclusions

The present paper systematically compared the impact of both sides of a baroclinic zonal jet in the growth of finite-amplitude surface cyclones using a two-layer quasigeostrophic model. The numerical experiments consisted in initially embedding localized cyclones at the lower and upper layer in various basic flows in such a way that cyclones interact baroclinically with each other. The first step consisted in systematically analyzing the impact of cyclonic and anticyclonic uniform background shears on the eddy kinetic energy budget at the lower layer over a large range of parameters. Basing on these results, the second step was dedicated to the dynamical understanding of the regeneration phase undergone by the lower-layer cyclone just after it crossed the upper-layer jet axis.

a. Instantaneous diagnoses

The decomposition of the omega equation permits identification of the distinct role played by the basic-state vertical shear, horizontal PV gradient, and horizontal shears on the vertical velocity as well as the role played by nonlinear terms.

- The presence of the basic-state vertical shear, as is well known, creates zones of convergence and divergence of the **Q** vector and thus ascending and descending motions respectively to the east and west of a cyclone (Sanders and Hoskins 1990). Therefore, the lower-layer cyclone should be located to the east of an upper cyclone to increase its vorticity via the stretching term. The effect of a poleward-oriented vertically averaged PV gradient (such as the planetary vorticity gradient or the relative vorticity gradient due to meridionally confined jets) is to diminish the ascending motions above the lower-layer cyclone, to decrease the stretching term there, and thus to diminish the lower-layer vorticity growth. From a kinetic energy perspective, the vertically averaged PV gradient mainly enhances the vertical redistribution of energy, which primarily transfers energy from the lower to upper layer. On the contrary, the vertical shear favors large internal conversion rates, a prime source of kinetic energy for both the lower and upper layers during baroclinic interaction. Since the vertical redistribution term of kinetic energy is mainly anticorrelated with the internal conversion rate in the lower layer, the computation of their sum is needed to estimate the kinetic energy evolution. This sum has an insightful formulation since it is the product of the perturbation stretching term $f_0 \partial \omega' / \partial p$ by the opposite of the perturbation streamfunction $-\psi'$, which can be directly linked to the classical vorticity stretching arguments (Holton 1992).
- Horizontal shears also exert a direct influence on the omega equation. When the barotropic shear is increased, ascending motions due to the presence of the upper-layer cyclone are displaced on its northeastern side for cyclonic shears and on its southeastern

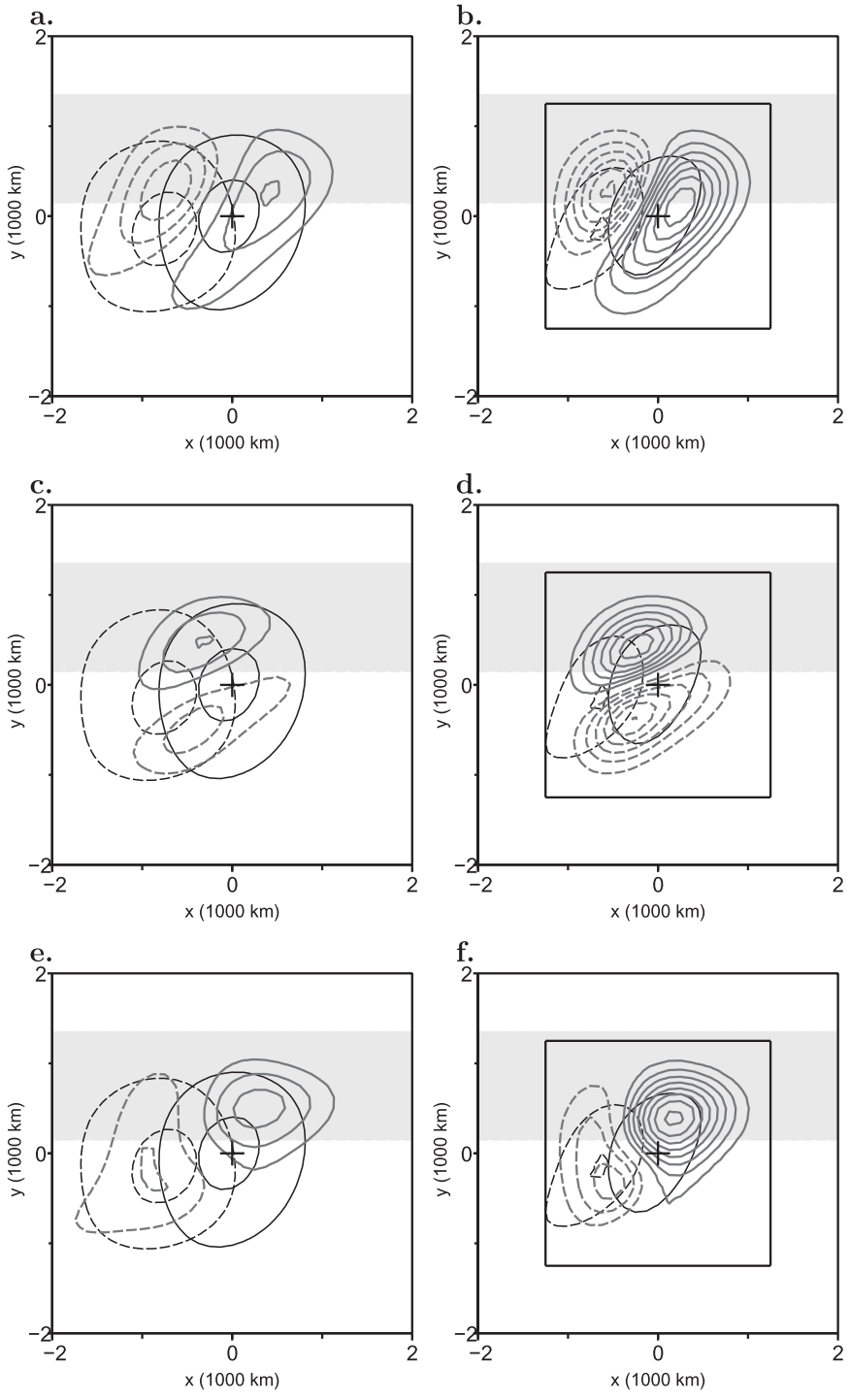

FIG. 10. Upper-level disturbances (black dashed contours) and lower-level disturbances (black solid contour) for the run with a meridionally confined jet before the jet-crossing phase ($t = 12$ h). The black contours correspond to (left) the perturbation streamfunction (contour interval $10^7\,\mathrm{m^2\,s^{-1}}$, negative values only) and (right) the perturbation vorticity (contour interval $5 \times 10^{-5}\,\mathrm{s^{-1}}$, positive values only). The gray contours in the left column represent (a) the linear part, (c) the nonlinear part, and (e) the total of the stretching term $-\lambda^{-1} s\omega'_{u-l}$ (contour interval $2 \times 10^{-10}\,\mathrm{s^{-2}}$). The gray contours in the right column represent (b) the linear part, (d) the nonlinear part, and (f) the total of the sum $[\mathrm{CV} + \mathrm{CI}/2]/\langle K'_l \rangle_S$ (contour interval $2 \times 10^{-4}\,\mathrm{m^2\,s^{-3}}$). The light gray band represents values of the basic-state lower-layer zonal wind $>$ $20\,\mathrm{m\,s^{-1}}$. The black square represents the area S over which energy growth rates are computed.

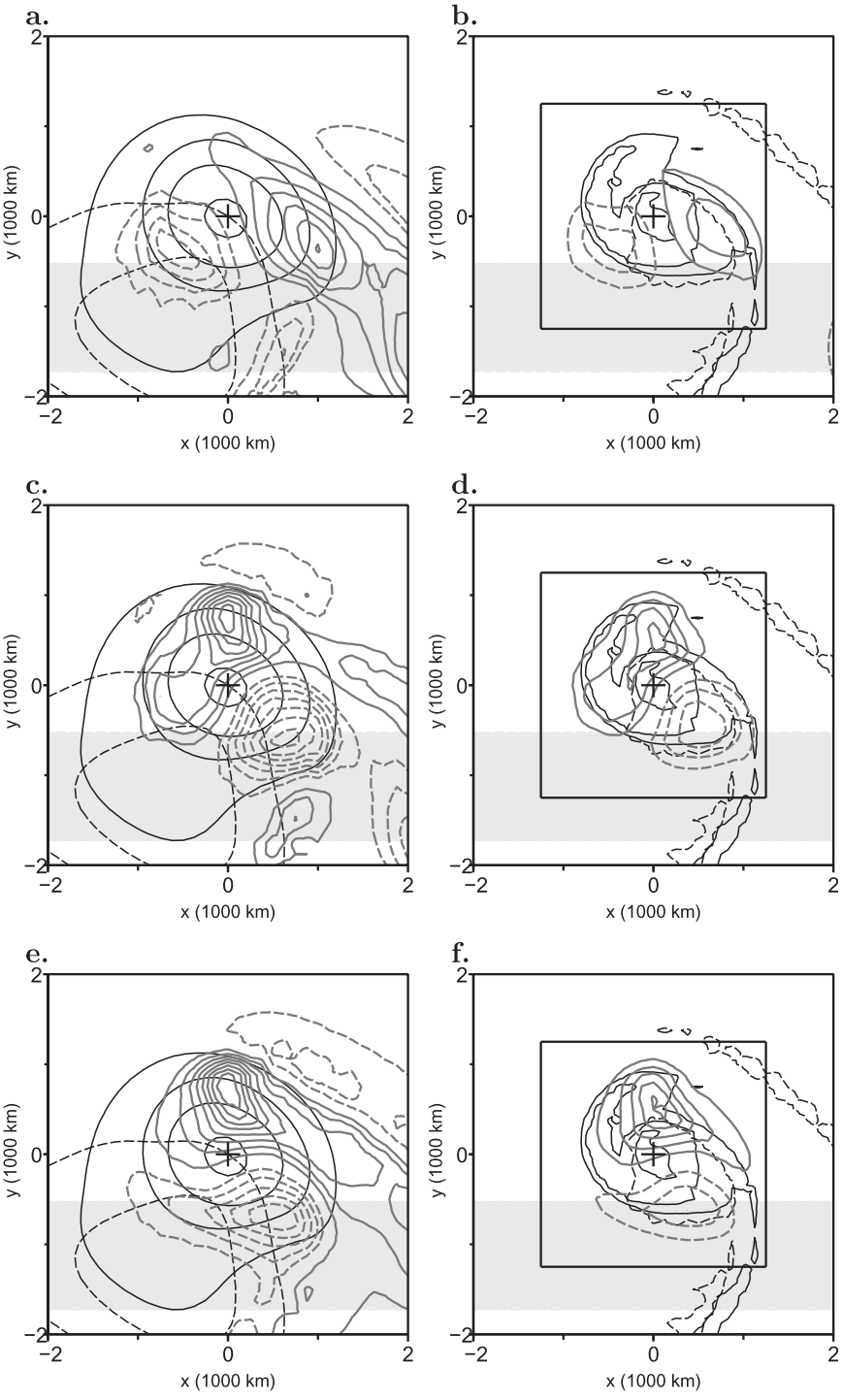

FIG. 11. As in Fig. 10, but after the jet-crossing phase ($t = 54$ h).

side for anticyclonic shears. The converse occurs when the upper-layer shear is increased keeping constant the lower-layer shear. The direct effects of the horizontal shears in the omega equation are thus not straightforward since they depend on the relative amplitude of the lower- and upper-layer shears.

- For isotropic cyclones, nonlinear terms in the kinetic energy budget do not create any asymmetry and therefore cannot lead to any net growth of the lower-layer kinetic energy. This symmetry is broken for elliptic vortices. Consider eddies that are horizontally stretched along the northeast–southwest direction,

which can be the result of the action of an anticyclonic background shear. If the upper-layer cyclone is upstream of the lower one, the nonlinearities lead to a net loss of eddy kinetic energy. In the case of a northwest–southeast horizontal tilt, which might be observed temporarily when vortices are embedded in a background cyclonic shear, the nonlinear forcing induces an increase in eddy kinetic energy.

b. *Evolution in uniform horizontal background shears*

Then, nonlinear simulations performed with linearly sheared zonal flows helped us to identify differences in the lower-layer cyclone growth between cyclonic and anticyclonic shears. As shown by Gilet et al. (2009), for the anticyclonic shear, the lower-layer cyclone maintains its position to the east of the upper one while this configuration is only transient for the cyclonic shear. This has several implications in the energy budget. (i) The anticyclonic shear allows a much more efficient and sustainable conversion of background potential energy to eddy potential energy through baroclinic interaction than the cyclonic shear for almost the whole range of the parameters. (ii) The anticyclonic shear allows a more important internal conversion rate from eddy potential to eddy kinetic energy than the cyclonic shear. (iii) In the presence of large barotropic horizontal PV gradient, the vertical redistribution of kinetic energy is enhanced in the anticyclonic shear and leads to a greater upward transfer of kinetic energy than in the cyclonic shear. Finally, changes in the horizontal shape of the cyclones also modify barotropic conversion terms. While they are moderately stretched and do not maintain any fixed orientation in the cyclonic shear, they are vigorously horizontally stretched along the dilatation axes in the anticyclonic shear. This leads to marginal barotropic conversion rates in the former case but strongly negative ones in the latter.

Determining which side of a zonal jet is more favorable to cyclones deepening is tantamount to quantitatively weighting the aforementioned effects, which all depend on the parameter range. Increasing vertical shears will favor more the growth on the anticyclonic side while increasing PV gradient will have the opposite effect. Generally speaking, the lower-layer kinetic energy growth is more sensitive to changes in horizontal shears in the anticyclonic case than in the cyclonic one but the effects of the upper- and lower-layer shears are opposite. Increasing the upper-layer shear increases the growth rates on the anticyclonic side while increasing the lower-layer shear decreases the growth on the anticyclonic side much more rapidly than on the cyclonic side. Increasing the two shears in the same way (i.e., adding a barotropic shear) is more favorable to the growth on the cyclonic side. Note finally that less sensitivity was found by changing the spatial scale and amplitude of the disturbances.

c. *Evolution in meridionally confined jets*

Finally, in the numerical experiments where the lower and upper cyclones were initially located on the warm side of a meridionally confined baroclinic zonal jet, the cyclones are shown to be able to cross the jet from their warm to cold sides (i.e., from their anticyclonic to cyclonic sides). Two peaks in the kinetic energy growth rates of the lower-layer cyclone, distinct in nature, were identified in that particular case, one before the jet-crossing phase and another after. The first peak is a result of the classical baroclinic interaction, which involves the linear part of the vertical velocity that is induced by the presence of eddies evolving in a baroclinic basic flow. The second peak is more complex. It is mainly driven by the nonlinear part of the vertical velocity and is totally determined by the three-dimensional structure of the disturbances when they reach the cyclonic side of the jet. It confirms the results found in the section dedicated to linearly-sheared zonal flows where nonlinear terms were found to favor the growth in the cyclonic shear.

d. *Perspectives*

This paper constitutes a new step toward our understanding of the regeneration process undergone by surface cyclones during the jet-crossing phase. In Rivière and Joly (2006), a real surface cyclone was shown to rapidly deepen during the jet-crossing phase via the same energy conversion term as in the present paper (i.e., the product of the stretching term by the perturbation streamfunction). Future studies will investigate the role of the nonlinear part of the stretching term in the deepening of such real winter storms. It would be also of particular interest to make a bridge between this decomposition into linear and nonlinear parts of the vertical velocity and the decomposition into its along- and cross-isentrope components (Keyser et al. 1992). It is particularly intriguing that the cross-isentrope component of the **Q** vector was shown to be important to understand the late stage of some real cyclones (Martin 2006, 2007) similarly to the nonlinear part at the end of our idealized life cycle. In the present study, the linear and nonlinear parts respectively exhibit zonally oriented and meridionally oriented dipoles of downdrafts and updrafts (e.g., see Figs. 11a,c), which are mainly parallel and perpendicular to the basic-flow isentropes. However, the basic-flow isentropes being very different

from the total-flow isentropes for mature cyclones, no direct link can be made between the two decompositions. More systematic analysis would be needed in future studies to clarify this aspect.

Acknowledgments. This work was funded by the CNRS/INSU/LEFE/IDAO project EPIGONE. The authors acknowledge the suggestions of the two anonymous reviewers that have helped to improve the presentation of the manuscript.

REFERENCES

Adem, J., 1956: A series solution for the barotropic vorticity equation and its application in the study of atmospheric vortices. *Tellus,* **8,** 364–372.

Baehr, C., B. Pouponneau, F. Ayrault, and A. Joly, 1999: Dynamical characterization and summary of the FASTEX cyclogenesis cases. *Quart. J. Roy. Meteor. Soc.,* **125,** 3469–3494.

Bjerknes, J., and H. Solberg, 1922: Life cycle of cyclones and the polar front theory of atmospheric circulation. *Geofys. Publ.,* **3,** 1–18.

Cai, M., and M. Mak, 1990: On the basic dynamics of regional cyclogenesis. *J. Atmos. Sci.,* **47,** 1417–1442.

Davies, H. C., C. Schär, and H. Wernli, 1991: The palette of fronts and cyclones within a baroclinic wave development. *J. Atmos. Sci.,* **48,** 1666–1689.

Gilet, J.-B., M. Plu, and G. Rivière, 2009: Nonlinear baroclinic dynamics of a surface cyclone crossing a zonal jet. *J. Atmos. Sci.,* **66,** 3021–3041.

Holland, G., 1984: Tropical cyclone motion: A comparison of theory and observation. *J. Atmos. Sci.,* **41,** 68–75.

Holton, J., 1992: *An Introduction to Dynamic Meteorology.* 3rd ed. Academic Press, International Geophysics Series, Vol. 48, 511 pp.

Hoskins, B. J., and P. J. Valdes, 1990: On the existence of storm-tracks. *J. Atmos. Sci.,* **47,** 1854–1864.

——, I. Draghici, and H. C. Davies, 1978: A new look at the ω-equation. *Quart. J. Roy. Meteor. Soc.,* **104,** 31–38.

James, I., 1987: Suppression of baroclinic instability in horizontally sheared flows. *J. Atmos. Sci.,* **44,** 3710–3720.

Keyser, D., B. Schmidt, and D. Duffy, 1992: Quasigeostrophic vertical motions diagnosed from along- and cross-isentrope components of the **Q** vector. *Mon. Wea. Rev.,* **120,** 731–741.

Martin, J. M., 2006: The role of shearwise and transverse quasi-geostrophic vertical motions in the midlatitude cyclone life cycle. *Mon. Wea. Rev.,* **134,** 1174–1193.

——, 2007: Lower-tropospheric height tendencies associated with the shearwise and transverse components of quasigeostrophic vertical motion. *Mon. Wea. Rev.,* **135,** 2803–2809.

Morel, Y., and J. McWilliams, 1997: Evolution of isolated interior vortices in the ocean. *J. Phys. Oceanogr.,* **27,** 727–748.

Moustaoui, M., H. Teitelbaum, C. Basdevant, and Y. Boughaleb, 2002: Linked behavior of twin tropical cyclones. *J. Geophys. Res.,* **107,** 4378, doi:10.1029/2000JD000066.

Oruba, L., G. Lapeyre, and G. Rivière, 2012: On the northward motion of midlatitude cyclones in a barotropic meandering jet. *J. Atmos. Sci.,* **69,** 1793–1810.

——, ——, and ——, 2013: On the poleward motion of midlatitude cyclones in a baroclinic meandering jet. *J. Atmos. Sci.,* **70,** 2629–2649.

Phillips, N., 1951: A simple three-dimensional model for the study of large-scale extratropical flow patterns. *J. Meteor.,* **8,** 381–394.

Pinto, J., S. Zacharias, A. H. Fink, G. Leckebusch, and U. Ulbrich, 2009: Factors contributing to the development of extreme North Atlantic cyclones and their relationship with the NAO. *Climate Dyn.,* **32,** 711–737.

Rivière, G., 2008: Barotropic regeneration of upper-level synoptic disturbances in different configurations of the zonal weather regime. *J. Atmos. Sci.,* **65,** 3159–3178.

——, and A. Joly, 2006: Role of the low-frequency deformation field on the explosive growth of extratropical cyclones at the jet exit. Part I: Barotropic critical region. *J. Atmos. Sci.,* **63,** 1965–1981.

——, B. L. Hua, and P. Klein, 2001: Influence of the beta-effect on nonmodal baroclinic instability. *Quart. J. Roy. Meteor. Soc.,* **127,** 1375–1388.

——, ——, and ——, 2004: Perturbation growth in terms of baroclinic alignment properties. *Quart. J. Roy. Meteor. Soc.,* **130,** 1655–1673.

——, P. Arbogast, G. Lapeyre, and K. Maynard, 2012: A potential vorticity perspective on the motion of a mid-latitude winter storm. *Geophys. Res. Lett.,* **39,** L12808, doi:10.1029/2012GL052440.

Rossby, C. G., 1948: On displacements and intensity changes of atmospheric vortices. *J. Mar. Res.,* **7,** 175–187.

Sanders, F., and B. J. Hoskins, 1990: An easy method for estimation of Q-vectors from weather maps. *Wea. Forecasting,* **5,** 346–353.

Schultz, D., D. Keyser, and L. Bosart, 1998: The effect of large-scale flow on low-level frontal structure and evolution in midlatitude cyclones. *Mon. Wea. Rev.,* **126,** 1767–1791.

Shapiro, M., and D. Keyser, 1990: Fronts, jet streams and the tropopause. *Extratropical Cyclones: The Erik Palmén Memorial Volume,* C. W. Newton and E. O. Holopainen, Eds., Amer. Meteor. Soc., 167–191.

Thorncroft, C. D., B. J. Hoskins, and M. McIntyre, 1993: Two paradigms of baroclinic-wave life-cycle behaviour. *Quart. J. Roy. Meteor. Soc.,* **119,** 17–55.

Vallis, G., Ed., 2006: *Atmospheric and Oceanic Fluid Dynamics.* Cambridge University Press, 745 pp.

Wernli, H., R. Fehlmann, and D. Luthi, 1998: The effect of barotropic shear on upper-level induced cyclogenesis: Semi-geostrophic and primitive equation numerical simulations. *J. Atmos. Sci.,* **55,** 2080–2094.

——, S. Dirren, M. A. Liniger, and M. Zillig, 2002: Dynamical aspects of the life cycle of the winter storm 'Lothar' (24–26 December 1999). *Quart. J. Roy. Meteor. Soc.,* **128,** 405–429.

Whitaker, J., and A. Barcilon, 1992: Type B cyclogenesis in a zonally varying flow. *J. Atmos. Sci.,* **49,** 1877–1892.